Features of dominant mesoscale variability, circulation patterns and dynamics in the Strait of Sicily

P.F.J. Lermusiaux*, A.R. Robinson

Division of Enginerring and Applied Sciences, Harvard University, Pierce Hall G2A, 29 Oxford Street, Cambridge, MA 02138, USA

Abstract

Combining an intensive hydrographic data survey with a numerical primitive equation model by data assimilation, the main features of dominant mesoscale to subbasin-scale variability in the Strait of Sicily (Mediterranean Sea) during the summer of 1996 are estimated, revealed and described, and several hydrographic and dynamical properties of the flow and variabilities discussed. The feature identification is based on two independent real-time analyses of the variability. One analysis "subjectively" evaluates and studies physical field forecasts and their variations. The other more "objectively" estimates and forecasts the principal components of the variability. The two independent analyses are found to be in agreement and complementary. The dominant dynamical variations are revealed to be associated with five features: the Adventure Bank Vortex, Maltese Channel Crest, Ionian Shelfbreak Vortex, Messina Rise Vortex, and temperature and salinity fronts of the Ionian slope. These features and their variations are found to have links with the meanders of the Atlantic Ionian Stream. For each feature, the characteristic physical scales, and their deviations, are quantified. The predominant circulation patterns, pathways and transformations of the modified Atlantic water, Ionian water and modified Levantine intermediate water, are then identified and discussed. For each of these water masses, the ranges of temperature, salinity, depth, velocity and residence times, and the regional variations of these ranges, are computed. Based on the estimated fields and variability principal components, several properties of the dynamics in the Strait are discussed. These include: general characteristics of the mesoscale anomalies; bifurcations of the Atlantic Ionian Stream; respective roles of topography, atmospheric forcings and internal dynamics; factors controlling (strengthening or weakening) the vortices identified; interactions of the Messina Rise and Ionian Shelfbreak vortices; and, mesoscale dynamics and relatively complex features along the Ionian slope. For evaluation and validation of the results obtained, in situ data, satellite sea surface temperature images and trajectories of

---

*Corresponding author. Tel.: + 1-617-495-0378; fax: + 1-617-495-5192.

E-mail address: pierrel@pacific.harvard.edu (P.F.J. Lermusiaux).

surface drifters are employed, as well as comparisons with previous studies.

1. Introduction

During the stratified period, the upper-ocean Atlantic Ionian Stream (AIS) enters the Strait of Sicily from the western Mediterranean, often meanders due to topographic effects, internal baroclinic processes or strong atmospheric forcings, and then exits into the upper eastern Mediterranean, usually bifurcating as it passes the slope of the Ionian Sea. Within the Strait, there are vortices and eddies, some of which are associated with the meanders of the AIS. In upper layers, the modified Atlantic water (MAW) flows from west to east, mainly transported by the AIS. In intermediate and deep layers, the modified Levantine intermediate water (abbreviated next by LIW) flows from east to west. Additional intrusions of waters from the Ionian Sea, mostly of properties intermediate between the MAW and LIW, also occur, and there are important horizontal and vertical mixing processes. The features of the circulation in the Strait have their own complex dynamics. The meanders and eddies vary in strength, size and shape, shift positions and interact, being only partly controlled by topographic features, coastal geometry and thermohaline boundary forcings.

During August and September 1996, an intensive data set was acquired from the N.R.V. Alliance and several aircraft surveys, providing a nearly synoptic time-series for the Strait of Sicily region. Assimilating these data into a numerical primitive equation (PE) model, we nowcasted and forecasted the regional variability (see Section 1.2). From these estimates, we found and analyzed in real-time several surface-intensified features of dominant mesoscale variability, as schematized on Fig. 1. We did this "subjectively", by evaluating and carefully looking at variations of ocean field estimates. At the same time and independently, we more "objectively" organized the variability into multivariate and evolving principal components. The present work first describes these two analyses, their agreement and their complementarity. Results obtained from simulations carried out after the real-time forecasting are then presented. Important circulation patterns, water pathways and hydrographic features are revealed, and several dynamical properties of the flow and variabilities discussed.

The Strait of Sicily region has been researched extensively, especially recently (see Section 1.1). Most studies to date have focused on specific processes and have been local, either in space or time, based on cross-section, time-series, coastal or surface observations. These local hydrographic, current or ecosystem data have been collected by various platforms and sensors, including ships, drifters, satellites and moorings. In the context of this accumulated knowledge and new 1996 intensive data set, a comprehensive identification and study of the features of dominant variability in the Strait can be initiated, using methods that combine observations with four-dimensional (space and time) dynamics. The present work focuses on the mesoscale to subbasin-scale variability and dynamics of the summer circulation north of 34N.
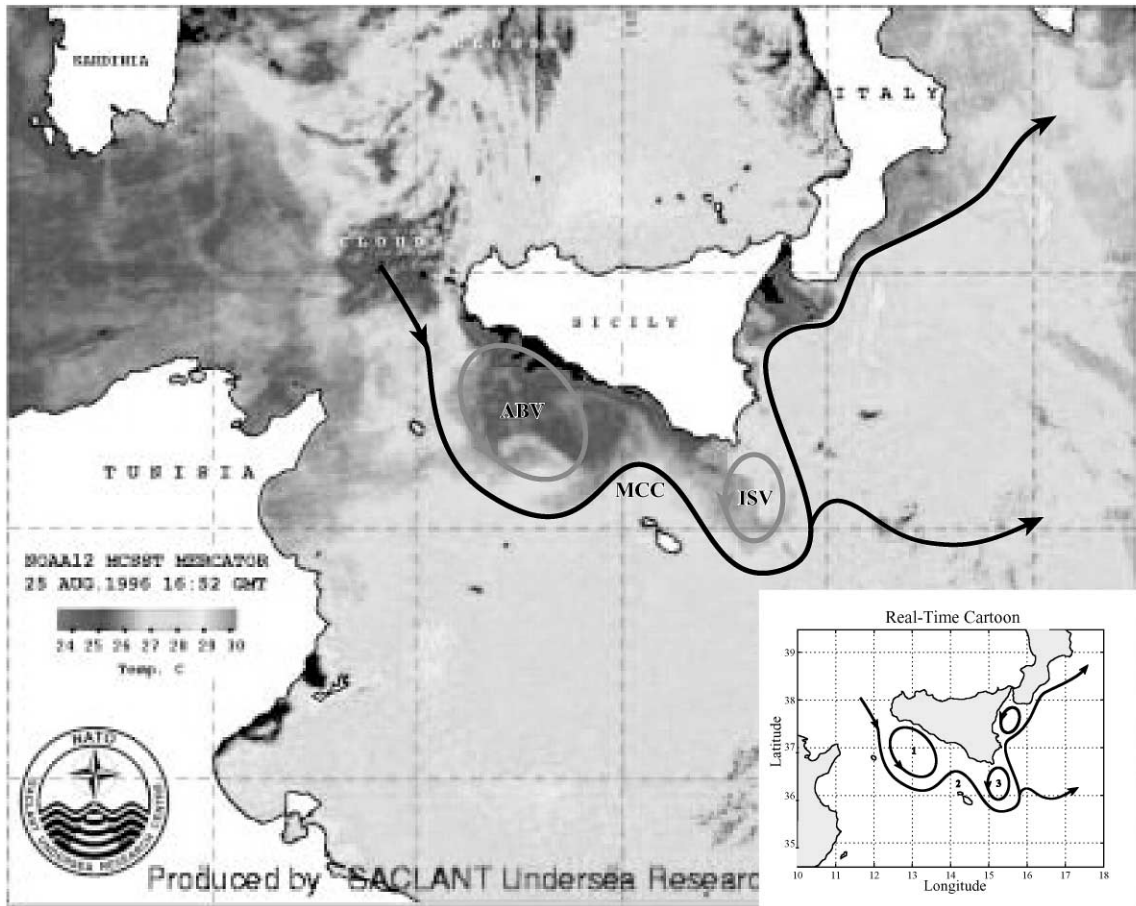
Fig. 1. Cartoon of the summer surface circulation features identified by Robinson et al. (1998b) for the Strait of Sicily region (De Agostini, 1998). It is superposed on the satellite sea surface temperature (SST) distribution for Aug. 25, 1996 (Saclantcen). The cartoon drawn in real-time in the scientific notebook is shown in the bottom-right corner (it was scanned and cleaned for clarity).

1.1. Physical variability in the Strait of Sicily: overview of recent progress

The Strait of Sicily region corresponds to the narrow passageway connecting the large western and eastern Mediterranean basins (Fig. 2). Prior to the 1996 field work, some elements of the circulation were known, based on direct measurements, modeling studies or their combination; for comprehensive reports, we refer to Grancini and Michelato (1987), Manzella et al. (1988), Robinson et al. (1991, 1999), Moretti et al. (1993), and Manzella (1994). Advected eastward in upper layers by the AIS, the fresh MAW meanders and mixes in the Strait before reaching the Ionian. In intermediate and deep layers, below the AIS, the salty LIW enters the Strait from the Ionian, usually within the sills south of Malta (Fig. 2). The LIW core was observed in this region around 250–450 m, slowly and broadly flowing westward. The regional characteristics of water pathways

Raw Topogography AIS96 — Large Region (etopo 5)
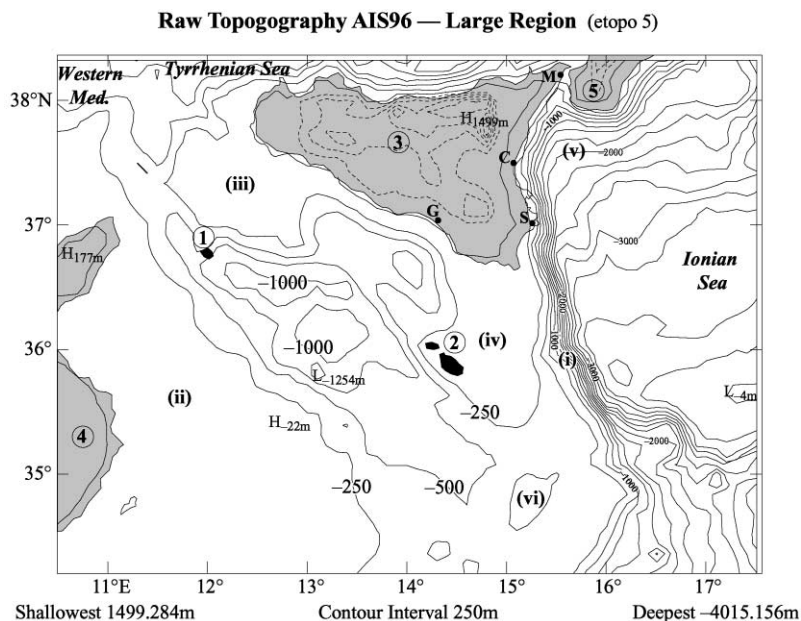
Fig. 2. Topography and geography of the Strait of Sicily region. The numbers indicate Pantelleria Island (1), Malta Island (2), Sicily (3), Tunisia (4) and Calabria (5). The (i)'s indicate topographic features (De Agostini, 1998): the Ionian slope (i), Tunisian shelf (ii), Adventure Bank (iii), Maltese plateau (iv), Messina Rise (v) and Medina Bank (vi). The letters indicate cities mentioned in the text: G for Gela, S for Siracusa, C for Catania and M for Messina.

were however not well known. Most investigations in the Strait have focused on the exchange between the Mediterranean basins. For recent reviews on the Mediterranean, we refer to Robinson and Malanotte-Rizzoli (1993), La Violette (1994a), Malanotte-Rizzoli and Robinson, (1994), Robinson and Golnaraghi (1994), Pinardi and Roether (1998), Gacic et al. (1999) and Lipiatou et al. (1999).

   In the Strait, the variability occurs at several time and space scales (Grancini and Michelato, 1987; Manzella et al., 1990; Moretti et al., 1993; Robinson et al., 1999), and involves interactions of several water masses (Warn-Varnas et al., 1999). At the interannual scales (Pinardi et al., 1997; La Violette, 1994b) and seasonal scales (Manzella et al., 1988; Manzella and La Violette, 1990; Manzella, 1994; Astraldi et al., 1999), the variations in the MAW and LIW transports through the Strait have been used to monitor the variability of the Mediterranean and its basins. For both the MAW and LIW, the averaged kinetic variability has been observed 2 to 4 times higher in winter than in summer, in response to stronger wind stress and reduced stratification (Grancini and Michelato, 1987; Manzella et al., 1988, 1990; Onken and Sellschopp, 1998). The hydrographic properties of the MAW are also known to undergo significant seasonal variations, but those of the LIW are more constant (Manzella et al., 1990; Moretti et al., 1993). At the subbasin-scale and mesoscale, baroclinic processes have been found important at several locations (Grancini and Michelato, 1987; Onken and Sellschopp, 1998), in accord with the two-layer exchange of MAW and LIW. Using a series of weekly sea surface temperature (SST) satellite images during 1992,

Borzelli and Ligi (1999a, b) recently reported that the scales of a week to two months and of 40 to 300 km prevail at the surface, which further supports the relevance of mesoscale to subbasin-scale phenomena.

At weather time-scales, in relation to the frequency of passing storms, a substantial oceanic response has been found in the 4–10 d periods, especially on the continental shelves (Grancini and Michelato, 1987; Manzella et al., 1990). South of Sicily, local upwelling events have often been observed (e.g. Philippe and Harang, 1982; Piccioni et al., 1988). The dynamic of these upwellings appears to be of several types (Ozturgut, 1975; Askari, 1998). It involves classic wind-driven coastal upwelling (Cushman-Roisin, 1994), but is also induced by inertia of the isopycnal domes of the AIS meanders and cyclonic vortices (Robinson et al., 1999). In fact, even though the cold filaments and frontal structures observed in summer by Philippe and Harang (1982) underwent strong variabilities, these authors noticed that the structures usually persisted until the winter. Finally, topographically induced upwelling along the shelfbreak south of Sicily can also occur, in response to either wind effects, direct advection by the AIS as it rises above the along-shore relief variations (e.g. Janowitz and Pietrafesa, 1982), or localized tidal mixing as along other shallow shelfbreaks (e.g. Simpson, 1998).

Dominant meanders for the AIS were reported to have time-scales of the order of 5–8 days (Manzella et al., 1988), in response to atmospheric, topographic and internal (e.g. stratification, inertia) forcings. Even though effects of these forcings have been observed in several localized areas, their combined and four-dimensional role in establishing circulation features has only been recently addressed (Robinson et al., 1999). At the western entrance of the Strait, Herbaut et al. (1998) have investigated the separation and inflow of the AIS, based on idealized sensitivity studies. Topographic Rossby modes (e.g. Miller et al., 1996), trapped by the coastline and sharp topographic gradients, were also suggested to occur in this region, with 2–5 days periods (Pierini, 1996). At the eastern side, near the Ionian shelfbreak, the mesoscale dynamics have not been studied extensively but are known to be complex (e.g. Grancini and Michelato, 1987); in particular, they involve meanders and bifurcations of the AIS (e.g. Briscoe et al., 1974; Robinson et al., 1999). Some light will be shed on these regional dynamics in Sections 4–7, emphasizing the roles of local frontal structures and steep topography.

The mixing of water masses is important. It has been attributed mainly to turbulent mixing in high shear zones, atmospheric forcings, and mesoscale eddies and instabilities (Warn-Varnas et al., 1999). At higher frequencies or smaller scales, tidal effects and internal waves can be locally significant (Grancini and Michelato, 1987; Artale et al., 1989; Mosetti and Purga, 1989; Molines, 1991). Semi-diurnal and diurnal tidal currents have been found largest along the Sicilian shelf, on the Adventure Bank and Maltese plateau (Fig. 2), with maximum velocities reaching 10 cm/s. Askari (1998) has observed local internal wave packets likely due to tidal forcing over the steep and shallow shelfbreaks of the Maltese plateau. During the summer, inertial oscillations have not been observed, except on the Adventure Bank (Artale et al., 1989) and at the Ionian shelfbreak especially near the Tunisian and Libyan shelves (Grancini and Michelato, 1987). Recently, Candela et al. (1999) reported short period (minutes to hours) gravitational and barotropic oscillations trapped by topography at the western entrance of the Strait and indicated that these fast oscillations are likely excited by traveling atmospheric pressure fronts. None of these super-tidal frequencies are considered here.

1.2. *Rapid Response 1996*: *data acquisition and field estimation*

Variability analyses were first carried out in real-time within the North Atlantic Treaty Organization operation Rapid Response 96 (RR96). This experiment was designed to demonstrate a rapid environmental assessment in marine operations (Pouliquen et al., 1997). It included a collaborative effort between the SACLANT Undersea Research Center (Saclantcen) and Harvard to develop a mesoscale predictive and descriptive system (Robinson et al., 1998b, 1999; Warn-Varnas et al., 1999). Previous cruises had taken place in the region in November 1994 and October 1995. During RR96, several ships sampled the region, measuring salinity and temperature as functions of depth using CTDs (Conductivity–Temperature–Depth), XCTDs (Expendable CTDs) and XBTs (Expendable Bathythermographs). Aircraft rapidly deployed expandable temperature probes (AXBTs, Aircraft-deployed XBTs). The positions and values of the hydrographic data collected from August 12 to September 15, 1996, are shown on Fig. 3.

The physical variables are temperature, salinity, velocity and pressure. During RR96, they were dynamically evolved by the numerical PE model of the Harvard Ocean Prediction System (HOPS, Lozano et al., 1996; Robinson, 1999). Nowcasts (dynamically adjusted objective analyses of in situ observations) and forecasts (Sections 2 and 3) of physical fields were computed via data assimilation using the Optimal Interpolation (OI) and Error Subspace Statistical Estimation (ESSE) schemes (Lermusiaux, 1997, 1999a,b). The latter approach is based on a reduction of the evolving statistics of interest to their dominant components or subspace (Sections 2 and 4). Combining dynamics with data, error statistics or variability properties are estimated, quantitatively organized and reduced as a function of importance (e.g. variance). In a sense, this approach connects the dynamical normal mode decomposition (e.g. Kundu, 1990; Monin, 1990) with the empirical orthogonal function (EOF) representation of data (e.g. Preisendorfer, 1988; von Storch and Frankignoul, 1998). One outcome is the four-dimensional forecast and principal component decomposition of the uncertainty or variability of ocean fields (Section 4). The operational procedures employed during RR96 for field initialization (e.g. use of historical synoptic data to obtain features statistically adequate for August) and forecast are described in Sellschopp and Robinson (1997) and Robinson et al. (1998b, 1999). The procedures for parallel error forecast, data assimilation and adaptive sampling are in Lermusiaux (1997, 1999b).

Fig. 3. (a): Coordinates of hydrographic profiles collected during the period Aug. 12–Sep. 15 of Rapid Response 1996, as provided by Sellschopp et al., Saclantcen. (b) *T/S* diagram of the (X)CTD data. Four ranges of depths were chosen so as to differentiate *T/S* zones in the upper layers. (c) as (b), but zooming on denser and deeper waters. See text for details.

The maximum depth for the XBTs is 750 m and for the XCTDs, 1000 m. The CTDs are lowered as close as possible to the bottom. The deepest in situ profile reaches 3200 m (the eastern-most CTD). For reference, the boundaries of the numerical domain (Fig. 2) are drawn on Fig. 3a. Note that there is no in situ data near the southwest corner of the domain (south of 34.5N, west of 12E). In that corner, field estimates tend toward climatological summer conditions (MODB data, e.g. Brankart and Brasseur, 1996).

AIS96 : (X)CTD and (A)XBT data, Aug 12−Sep 15 1996

(a)

(X)CTD data, Aug 12-Sep 15 1996

(b)

(X)CTD data, Aug 12-Sep 15 1996

(c)
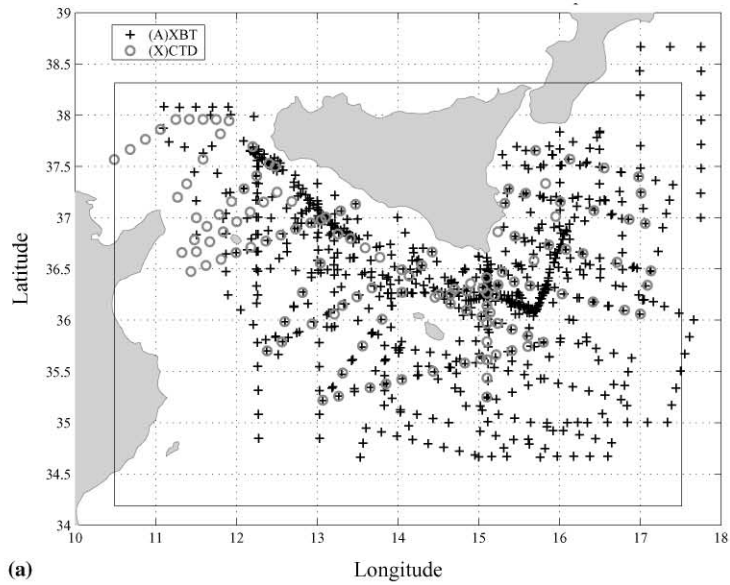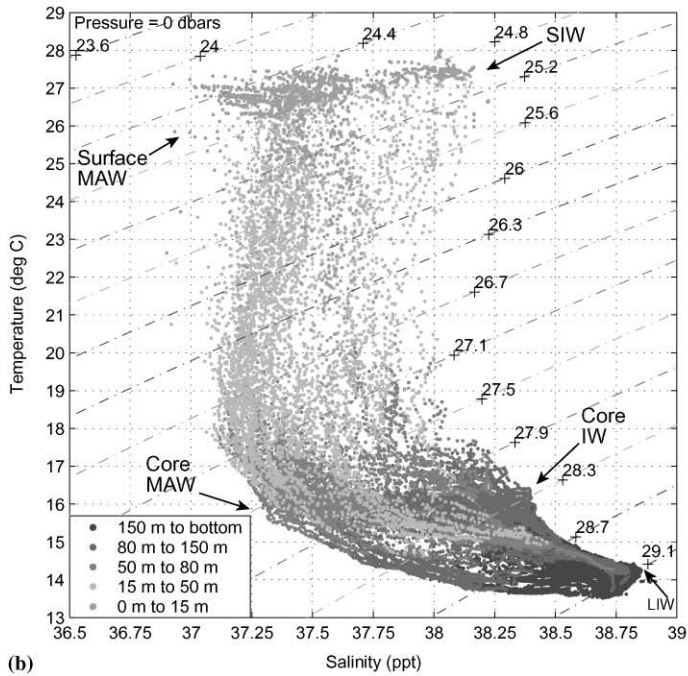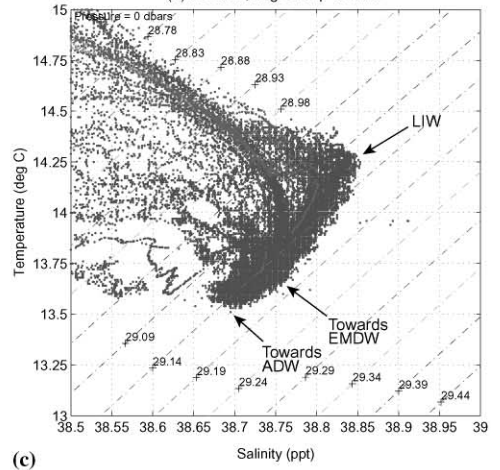
2. Parameters and methodologies

2.1. Data

The along-track spacing between stations is within 15–30 km for both the ship and flight surveys (Fig. 3a). Track plans were first based on the knowledge acquired during the 1994–95 cruises (Robinson et al., 1998b, 1999). Once the main features were established by data assimilation, sampling patterns for aircraft and ships were adaptive (e.g. Robinson and Glenn, 1999): they were designed in real-time based on predictions of fields and errors, and on intuition for the regions in which stations were expected to be most useful. On Fig. 3a, the adaptive samplings are the AXBT flight patterns and the return path of the N.R.V. Alliance from east to west (CTD stations overall parallel to the southern coast of Sicily, about 50 km offshore). On Sep. 15, the data set accumulated 926 profiles: 135 (X)CTDs and 791 (A)XBTs.

During RR96, the main water masses (see CTD data on Figs. 3b and c) consist of the upper-layer MAW and Ionian water (IW), mid-depth to bottom LIW, and transitions towards abyssal Eastern Mediterranean Deep Water (EMDW) and Adriatic Deep Water (ADW). This agrees with a compilation of previous observations (Grancini and Michelato, 1987; Manzella et al., 1990; Moretti et al., 1993; Artegiani et al., 1997; Malanotte-Rizzoli et al., 1997; Warn-Varnas et al., 1999; Astraldi et al., 1999). In summer, the surface heating leads to a broad scattering towards high temperatures. One can then distinguish the surface MAW and so-called SIW (surface Ionian water, Nittis et al., 1993) from the core MAW and IW. These summer surface waters are usually within 0 to 15 m (Fig. 3b) and have a relatively limited influence on the 3D circulation. Below, the surface stratification creates a transition layer ($\sim$15–50 m) to the core MAW ($\sim$40–80 m, 15–17°C, 37.2–37.8 PSU) and core IW ($\sim$70–150 m, 15–16.5°C, 37.8–38.4 PSU). The peak of the IW is marked clearly, near 16.5°C, 38.4 PSU (Fig. 3b). In comparison to the core MAW, the core IW is saltier, either warmer or cooler depending on position, but often heavier and deeper, in accord with excess evaporation and mixing of waters in the Ionian basin. Below these waters, there is a transition layer to the LIW, either the "MAW-to-LIW" or "IW-to-LIW" transition (the "bottom" or "top" curved envelopes of the T/S diagram). The salinity extremum of the LIW is at about 14.25°C, 38.85 PSU. For the profiles in the Ionian, below the LIW, there is a transition towards bottom EMDW or ADW.

2.2. AXBT salinity

Each AXBT temperature profile was complemented with estimated profiles of salinity and of its error. The method to do so (Lermusiaux, 1997) uses the CTD data (Fig. 3b) as a pool of reference temperature and salinity profiles. The salinities of a given AXBT, and their errors, are estimated using a three-dimensional, constrained and weighted average of the CTD salinities. The weights increase with the similarity between the location, date, depth, shape and range of the temperature profiles of the AXBT and reference CTDs. For a given depth and temperature, the constraints are weak (e.g. Sasaki, 1970): they only penalize departures of the estimated salinity from the average T/S diagram of the CTD data.

2.3. Models, boundary conditions and initialization

The dynamical model is the numerical PE model of HOPS (e.g. Robinson, 1996, 1997). Its physical state variables (Section 1.2) are the internal horizontal velocities $\hat{u}$, $\hat{v}$, barotropic transport stream function ψ and dynamical tracers, the temperature T and salinity S. The corresponding five fields are henceforth called the PE fields. The in situ data (Fig. 3a) were used to calibrate the diffusion parameters and boundary condition schemes. Atmospheric fluxes (wind stress, heat and fresh-water fluxes) based on the Fleet Numerical Meteorologic and Oceanographic Center data were imposed on top of a surface boundary-layer model combined with the PE. At the open-boundaries, radiation conditions based on the scheme of Orlanski (1976) and CFvN-type conditions of Spall and Robinson (1989) were employed. These conditions were selected based on calibration tests with the regional data. Open-boundary conditions have been utilized with HOPS for some time (e.g. Robinson and Leslie, 1985; Robinson and Walstad, 1987), and the schemes currently implemented are reviewed in Lermusiaux (1997). At coastal boundaries, the tangential flow was weakened using a Rayleigh friction, and the normal flow and tracer fluxes were set to zero. At the bottom, a simple boundary layer was employed, based on a drag coefficient and Rayleigh friction. It should be noted that, for numerical stability, the Ionian slope is somewhat more gentle than in reality: the position of the numerical shelfbreak is similar to that of Fig. 2, but the numerical slope extends to 17.5E (P.J. Haley, personal communication).

The gridded tracer fields were initialized by two-scale objective analysis of the data (Section 2), in two successive stages. The first stage maps the subbasin-scale tracer fields. The second stage adds the mesoscale correction to the subbasin-scale estimates. The horizontal correlations employed in these two analyses are "Mexican hats" (e.g. Louis et al., 1997), i.e. the negative of the second derivative of a two-dimensional Gaussian function, as often used for the Mediterranean (Robinson and Malanotte-Rizzoli, 1993). The initial flow is then computed from the tracer fields, also in two steps. A "first-guess" velocity is computed assuming geostrophic balance with the analyzed tracers, integrating the thermal-wind equations up and down from an approximate level of no motion. Acceptable depths for this level of no motion were here limited to the vertical extent of the pycnocline separating the MAW and LIW (on average over the numerical domain, from about 50 to 300 m). Within this acceptable range, the ultimate value was bracketed by choosing the depth leading to a subsequent dynamical adjustment of smallest amplitude (e.g. Milliff and Robinson, 1992). These first computations set the level of no motion at 180 m, which is near previous values (e.g. Grancini and Michelato, 1987; Moretti et al., 1993). The resulting approximate flow is a pre-conditioning for the second step: the "final estimate" of the initial velocity is obtained by carrying out a numerical momentum PE adjustment (e.g. Gill, 1982; Cane et al., 1998) of the first-guess velocity. Several dynamical effects are involved in this integration, including baroclinicity (e.g. deepening of the pycnocline towards Africa, mesoscale features), relief and diffusion (e.g. boundary layers). After adjustment, the initial velocity does not have a clear level of no motion. Although there are areas where horizontal velocities reverse direction (e.g. in some shallow shelf areas, above some LIW paths), usually at a depth near three-quarters of the local total depth, in many areas there are only significant changes, but no reversal, of direction. In fact, the level of minimum horizontal speed is at many locations within the bottom boundary layer.

2.4. Assimilation and variability forecasting

The assimilation approaches (e.g. Robinson et al., 1998a and references therein) are OI and ESSE. Each is used in the filtering mode, i.e. data are melded with the forecast as they become available, on a daily basis. For both schemes, after assimilation (a posteriori), the fields agree with the data and model within their respective error estimates. The OI consists of a two-scale objective analysis of the data, followed by a linear combination (blending) of the forecast and analyzed data (Lozano et al., 1996; Robinson et al., 1996). The blending involves a ramping in time of the analyzed data so as to account for temporal correlations and reduce possible dynamical shocks. The assimilation via ESSE is based on the reduction of the error statistics to their dominant multivariate components. This error subspace is initialized, forecast and used to assimilate data (Lermusiaux, 1999a, b; Lermusiaux and Robinson, 1999). Presently, statistical measures are based on a variance or least-squares criterion (Tarantola, 1987). A subspace reduction is then characterized by the dominant eigendecomposition of a (normalized when multivariate) covariance matrix. This approach is utilized in Section 4 to evolve the variability more objectively. The dominant eigendecomposition of the variability covariance matrix is initialized combining data and dynamics (Section 4.1), based on Lermusiaux et al. (2000). These spatial variability principal components and coefficients are then forecast via a Monte-Carlo approach (Section 4.2), modifying the size of the Monte-Carlo ensemble as a function of a convergence criterion.

3. Evaluation of field estimates and subjective variability

Quick-look "subjective" verifications of the variations of the predicted fields were carried out in real-time, from Aug. 22 until Sep. 7. Such evaluations require definitions for the error and its measure, i.e. the skill metric (e.g. Lynch et al., 1995). Errors are defined here as the differences between the forecasts and nature at the scales of interest (9 km and larger). Nature was assumed best represented by the nowcasts of the in situ data (objectively analyzed 3D fields, on days for which data were available, see Section 2) and satellite SST images (surface daily fields, E. Nacini, personal communication). For the nowcasts, an a posteriori error standard deviation is computed by HOPS and only regions of low error are used to evaluate forecasts. For the SST images, areas covered with clouds are masked but error fields are not provided: local uncertainties due to skin effects, daily cycles, blurs, etc., are thus interpreted, image by image. In general, forecast errors contain model and predictability errors (e.g. Daley, 1992). Both lead to phase errors and structural errors. Phase errors account for correct features evolving at the wrong place or time, e.g. vortex out of position. Structural errors account for approximate features at the right place and time, e.g. approximate meander shape. During RR96, the quick-look evaluation consisted of two steps: (i) identify the three-dimensional features of dominant variability, and (ii) assess the forecast quality based on the phase and structural adequacies of these features, by comparison with the nowcasts and satellite SST. There are iterations and feedbacks between these two steps. This is reflected in the results to follow: first, the overall properties of the fields are overviewed, then their quality evaluated, and finally, the features and their variations described for about 3 weeks.

3.1. Overview of dynamical fields

As seen on Fig. 4, surface temperatures are within 27–29°C, except north of Tunisia in the western Mediterranean and along the southern and eastern coast of Sicily where they are colder (about 24–26°C). In the Strait, the largest surface currents usually meander near the boundary between these surface temperatures (Figs. 4c and d). The upper-ocean inflow of MAW is mainly advected by these currents, the Atlantic Ionian Stream. During the present stratified and summer period, the AIS is strong and constrained towards Sicily, in a large part because winds are often westerly (e.g. Zavatarelli and Mellor, 1995; Angeluci and Pinardi, 1997), which maintains an upwelling front south of Sicily (Section 1.1). The 1996 subjective analyses (Figs. 4–6) indicated that, in the Strait, the AIS commonly meanders around three surface-intensified features (Fig. 1). The stream flows past Pantelleria on the north and bears northwestward around the Adventure Bank Vortex (ABV). It then turns southeastward in the Maltese Channel Crest (MCC), goes around the Ionian Shelfbreak Vortex (ISV) and finally flows off the shelf and bifurcates into the upper western Ionian Sea. The ABV, MCC and ISV were observed in real-time throughout the summer of 1996 and identified as the features associated with the dominant upper-ocean variability. The cyclonic vortex on the eastern side of Sicily (e.g. Fig. 4) was not studied in real-time because it was not in the main area of marine interests. However, the more objective study of Section 4 reveals that this vortex is energetically important, and its evolution and variations are thus described hereafter. As for the other features, it is named the Messina Rise Vortex (MRV) based on its topographic environment (Marani et al., 1993; De Agostini, 1998). In general, the variations of the phase and structure of these features (location in time and space, shape, strength, etc.) involved surface shifts of about 20–100 km, usually occurring within 2–4 days. This result is somewhat larger and faster than previously estimated based on local data (Section 1.1).

3.2. Quick-look evaluation

The subjective evaluations of the nowcasts and forecasts (Sellschopp and Robinson, 1997) are compiled in Tables 1–3. The evaluation of Fig. 4 correspond to the beginning (Aug. 22–25) of the period studied; this is to start a time-sequence which is continued in Section 3.3.

As summarized in Table 1 (line 1, Aug. 23) and Table 2 (line 1, Aug. 22), the SST image (Fig. 4a) and in situ nowcasts (Fig. 4c) compare well in the regions where in situ data are available (Fig. 3a). In both pictures, the ABV is of medium size, west of 14E and centered at (37N, 13E). The MCC is high: it almost reaches the coastline at (37N, 14.2E). Note that this explains why the offshore extension of the upwelling at the Gulf of Gela is often limited (Piccioni et al., 1988): the MCC forms a kinetic and potential energy barrier. The ISV is small, north of 36N and west of 15.75N. The MRV is masked by clouds on Fig. 4a, but, based on Fig. 4c, it is elongated from Calabria up to Siracusa (Fig. 2). The 3-day forecast for Aug. 25 (Fig. 4d) also compares well with the corresponding SST image (Fig. 4b), for all features (see scores on Table 3, line 1). As indicated on (Table 1, line 2), the ABV elongates and extends east to 14E, the MCC moves to the southeast and the ISV enlarges, strengthen and extends south. The MRV is still masked by clouds (Fig. 4b), but comparing Figs. 4c and d, it strengthens on its coastal sides and shifts its orientation to north–south. For the rest of the evaluation period, the agreement of the satellite SST and surface nowcasts is summarized by Tables 1 and 2, and the quality of the forecasts by the scores and comments in Table 3. Overall, the main
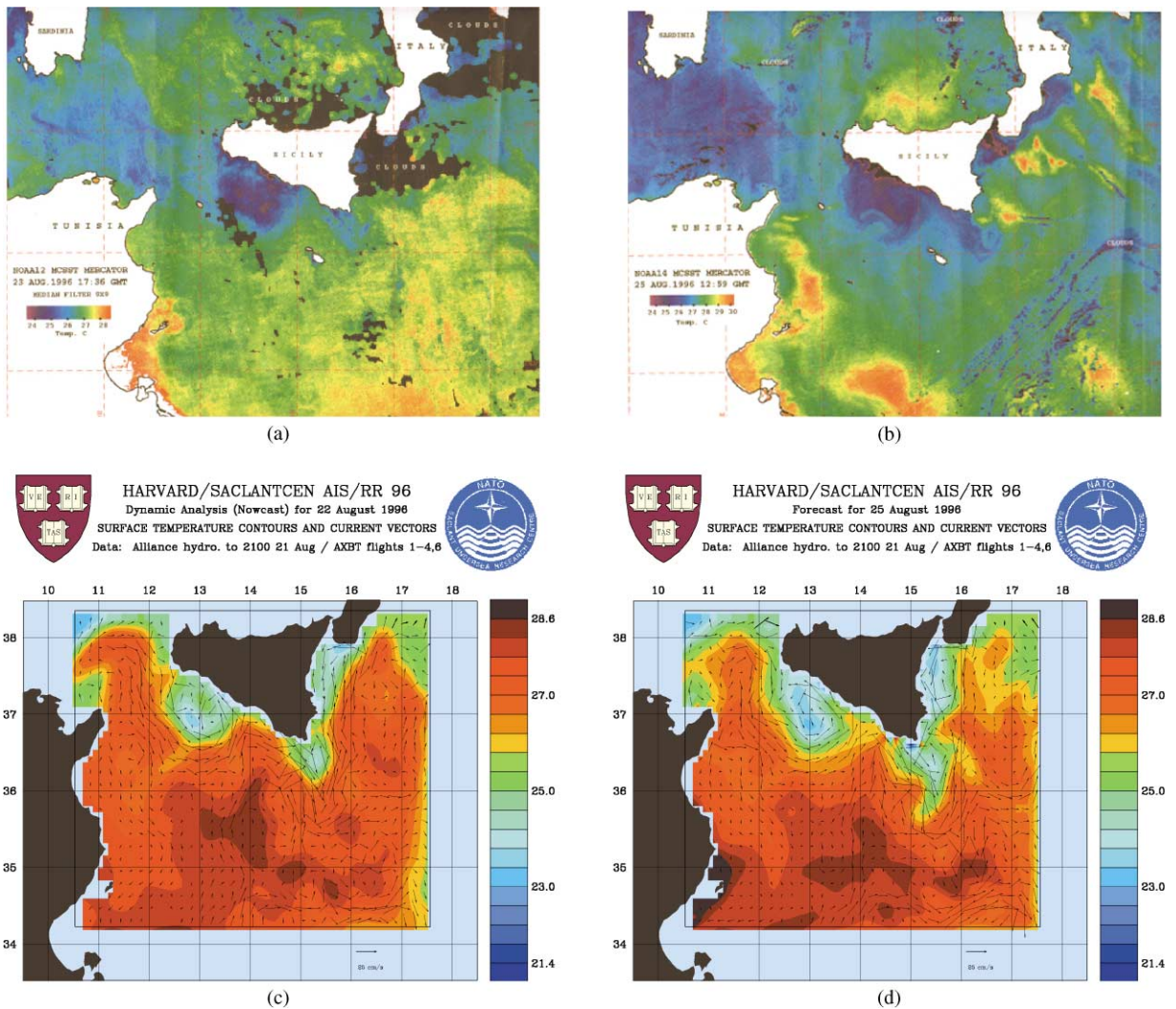
Fig. 4. Evaluation of nowcasts and forecasts. (a)–(b) satellite SST distributions for Aug. 23 and Aug. 25, 1996, respectively (see Table 1). (c) HOPS nowcast of the surface temperature for Aug. 22 (see Table 2), overlaid with surface velocity vectors (scale arrow is 0.25 m/s). (d) as (c), but for the forecast fields for Aug. 25 (see Table 3).

point is that the three types of field estimates are in relatively good accord. In particular, for the forecast skill, the comparisons of predicted versus nowcast developments for Aug. 25, Aug. 30, Sep. 3 and Sep. 7 indicate that the variations forecast are as nowcast about two times out of three.

3.3. Features of dominant variability

The features of dominant variability were identified subjectively by looking for the largest changes in surface temperature and velocity (e.g. Figs. 5 and 6). From this identification, the ABV,

Table 1
Satellite sea surface temperature

Date	Adventure Bank Vortex	Maltese Channel Crest	Ionian Shelfbreak Vortex
Aug. 23	Medium size W of 14 E	Close to Sicily, about 14.5E	Small, N of 36 N
Aug. 25	Extends E to 14 E	Moves to SE	Enlarges, extends S
Aug. 27	A little more to S	Similar to 23 Aug. moves N	Smaller or the same
Sept. 7	A little more to S Indented meander	Moves to SE as 25 Aug.	Extends E to 16E

Table 2
HOPS nowcasts (dynamic analysis of available in situ data)

Date	Adventure Bank Vortex	Maltese Channel Crest	Ionian Shelfbreak Vortex
Aug. 22	Medium size W of 14E	High centered 14 E	Small N of 36 N W of 15.75 E
Aug. 28	Square, moves E across 14 E	14.5 E Moves to SE	Enlarges, moves S, extends E
Aug. 31	Still straight on the W, moves N on the E	N at 14 E	Similar to 28 Aug.
Sept. 4	Similar to 22 Aug.	N at 14 E	Moves slightly NE

Table 3
HOPS forecasts for 2 or 3 days

Date	Adventure Bank Vortex	Maltese Channel Crest	Ionian Shelfbreak Vortex
Aug. 25	As nowcast + +	As nowcast + +	As nowcast + +
Aug. 30	Square but wrong orientation, +	Remains SE of 14 E −	Similar to nowcasts +
Sept. 3	Retains shape + +	N at 14 E + +	Slightly E −
Sept. 7	W edge moves W + +	Perhaps slight SE + +	Extends to S +

Table 1 overviews the variations of the three main features in the Strait, as observed in real-time from clear SST satellite images. Table 2 does the same, but using HOPS analyses of in situ data only. Table 3 scores (− to + +) and comments on the HOPS forecasts. For the regions of common coverage (cloud free locations with in situ data), the variations of the SST and HOPS nowcasts are often in accord with the corresponding HOPS predictions. The skill scores indicate that the 2-to-3-day forecasts had a success rate of around 70% (two times out of three, the variations forecast are as nowcast). Note that the four dates on the left vary with the Table. This is because SST images were used only when clear enough, nowcasts only when sufficient synoptic in situ data were collected, and forecasts were not always issued on nowcast days. However, fields a day apart can usually be compared since they were often observed synoptic; the dominant time scales of variability were usually longer, from a few days to a week.

MCC, ISV and MRV emerge. A posteriori, these features correspond to large volume variations of potential and kinetic energies (see Sections 4–7). Note that substantial variations in surface kinetic energy also occur along the Ionian slope, south of 36.5N (see Figs. 4–6), but they are challenging to identify subjectively. This is because the corresponding features and processes have complex three-dimensional variations, without large and relatively simple changes in surface T. The objective approach (Section 4) is thus more apt for their description.

3.3.1. Feature evolutions and variability

The fields shown on Fig. 5 (i.e. the in situ nowcasts for Aug. 28, Aug. 31 and Sep. 04, and dynamical forecast for Sep. 7) continue the time-sequence started on Figs. 4c and d (Aug. 22 and 25). Going from Aug. 25 (Fig. 4d) to Aug. 28 (Fig. 5a), the ABV becomes more square, somewhat smaller and moves slightly southeast, with its western side at 12.5E and its eastern side across 14E (the variations from Aug. 22 are summarized on Table 2, line 2; those from Aug. 25 to Aug. 27, based on the satellite SST, are on Table 1, line 3). The MCC is near 14.5E and flattens on its eastern side. The ISV is relatively large, but is weakening from Aug. 25 and moving east (from Aug. 22, it enlarges and moves south–southeast; Table 2, line 2). The MRV also weakens (warmer T), recovering the orientation north–northeast, parallel to the Sicilian coast. From Aug. 28 to Aug. 31 (Fig. 5b and Table 2, line 3), the ABV enlarges to the southwest on its west and moves north on its east. The MCC goes north, back to the coastline and 14E, while the ISV and MRV remain similar to what they were on Aug. 28. By Sep. 4 (Fig. 5c and Table 2, line 4), the ABV has returned to a position similar to that of Aug. 22 (Fig. 4c), its western side moving west and strengthening. The MCC also returns to the Aug. 22 situation, continuing to rise north at 14E, with its eastern side flattening along the coast. The ISV has moved slightly to the northeast and is weakening. The MRV remains relatively small and weak, excepted on its northern side which is slightly strengthening. Finally, by Sep. 7 (Fig. 5d and Table 3, line 4), the ABV continues to enlarge, its western edge moving west and its eastern edge east. The MCC moves slightly to the southeast. The ISV strengthens and extends south. The MRV becomes strong and oriented north–south, as on Aug. 25.

3.3.2. Tendencies and uncertainties

The surface tendencies (i.e. the differences between the HOPS fields plotted on Figs. 4 and 5) and the estimates of the error standard deviations of the in situ nowcasts (Fig. 6) quantify the above facts. For example, focusing on the variations from Aug. 22 to Aug. 28 (look at Fig. 6a and use Figs. 6e and f for error estimates), one confirms the squaring tendency of the ABV on its western side and the overall eastward motion of the ABV to 14E (on Fig. 6a, see extended positive T lobe near 12.5E and negative T lobe at 14E). One also notices the southeastward motion of the MCC (see negative lobe at 14E and positive lobe at 14.5E), the widening and eastward motion of the ISV (see positive T lobe at 15.2E), and the weakening and re-orientation of the MRV (see wide positive T lobe at 15.5E). Similar comments can be made for the other days. A limitation on the use of such differences of snapshots is that they are constrained by data coverage. They are also limited in number and correspond to distinct time spans. For all these reasons, they may not have sufficient statistical significance. A logical extension is a more objective methodology, which consist in estimating and evolving the dominant 3D principal components of the physical variability, combining data and dynamics in accord with their respective uncertainties (Section 4).
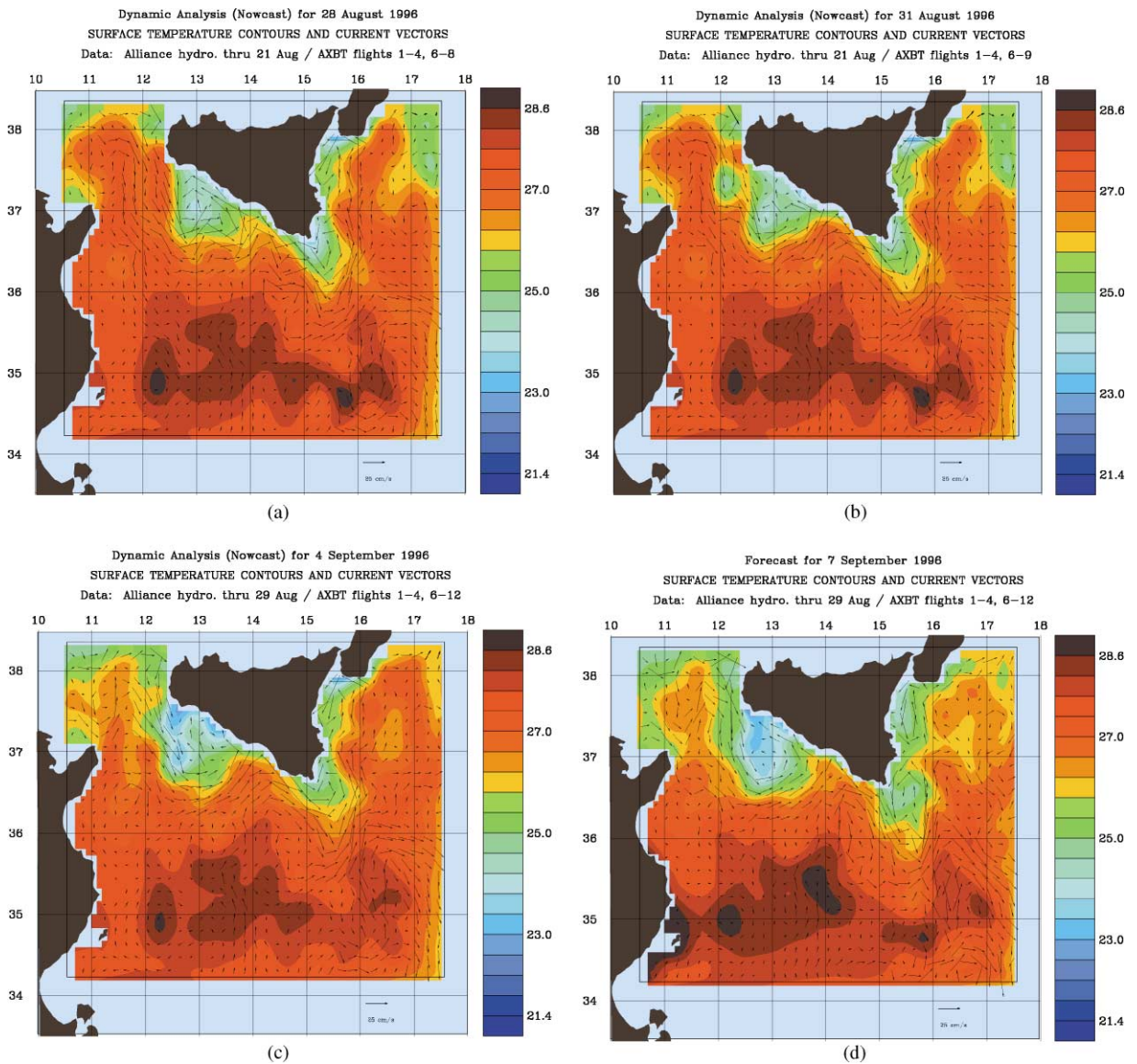
Fig. 5. (a) HOPS nowcast for Aug. 28, (b) for Aug. 31 and (c) Sep. 04. (d) HOPS forecast for Sep. 07. The surface temperatures are all overlaid with velocity vectors (scale arrow is 0.25 m/s).

3.3.3. Dynamics

The similarities between the surface temperature and flow fields on Sep. 7 (Fig. 5d) and Aug. 25 (Fig. 4d) are somewhat striking. This can be mainly explained by the fact that for 3 days before Aug. 25, wind estimates were mainly northwesterly and moderate (reaching 1 dyn/cm^2), while 3 days before Sep. 7, they were northwesterly to westerly and moderate to strong (1.25 dyn/cm^2 on

(a): Aug. 28–Aug. 22

(b): Aug. 31–Aug. 28

(c): Sep. 04–Aug. 31

(d): Sep. 07–Sep. 04

(e): Error Aug. 22 nowcast

(f): Error Aug. 28 nowcast

(g): Error Aug. 31 nowcast

(h): Error Sep. 04 nowcast
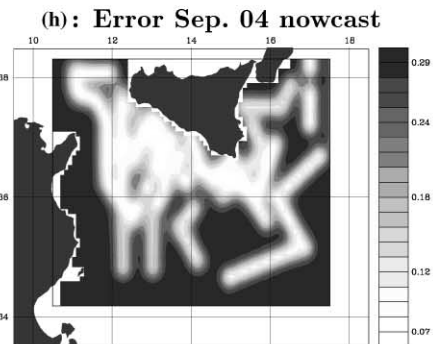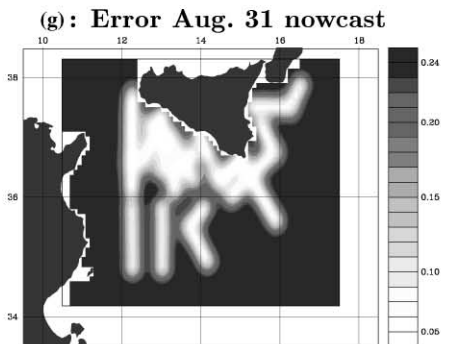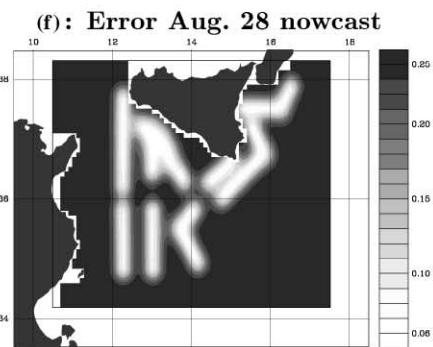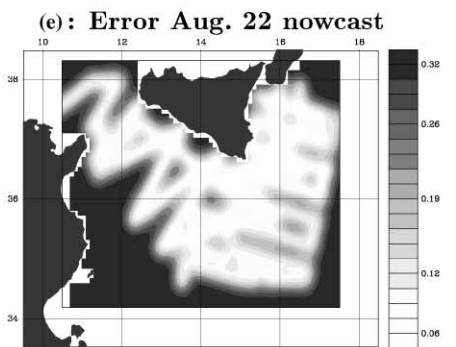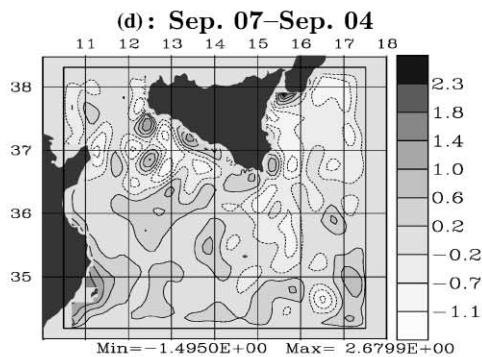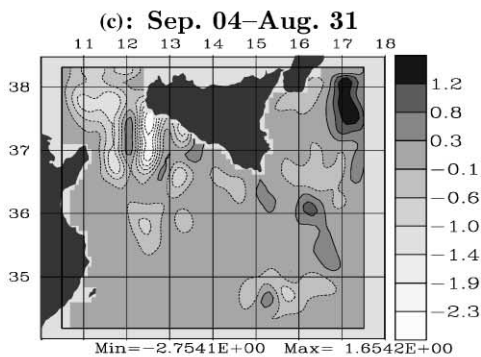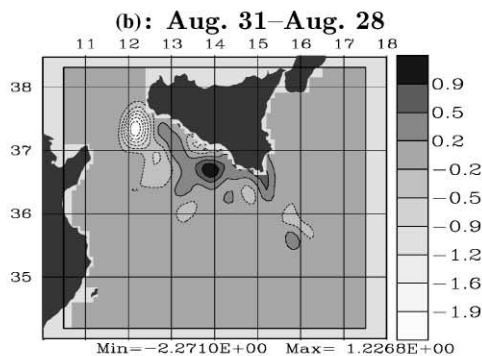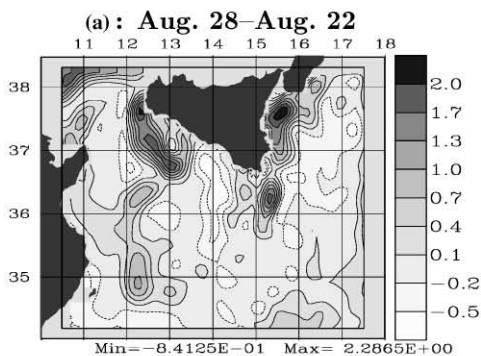
average). These two situations are analogous, and because of their duration, strength and orientation, the corresponding winds have a tendency to strengthen the AIS and to widen the ABV, MCC and ISV in both the along-shore and off-shore directions. This mainly explains the similarity between the two field snapshots after the wind events. However, during the rest of the time, including before Aug. 22 and Sep. 4 (also somewhat similar surface fields), the winds were estimated to be relatively weak and usually variable in direction. They could not have a substantial impact on the circulation features. The similarities between Aug. 22 and Sep. 4 are thus likely an artifact of internal dynamics, without correlations to the winds. This result is in accord with previous sea level data which indicated that several dynamical events are not related to local winds (Manzella et al., 1990).

From the above time-sequence, another overall observation is that the variations of the ISV and MRV often appear connected, over periods of days or more (see Figs. 4 and 5). This possibly indicates that the two vortices can be commonly influenced by dynamical processes occurring east of Sicily or along the Ionian slope, as will be discussed in Sections 4–6.

A last observation is that the AIS usually bifurcates when it reaches the Ionian slope (Figs. 4 and 5). One branch always advects MAW to the north along the slope, bordering the MRV and then the eastern side of Calabria. The other branch, however, is variable in strength and direction. During Aug. 22–28, it is strengthening and flowing east into the Ionian Sea, along 35.8N (Figs. 4 and 5). Beginning on Aug. 31 (Fig. 5b), it starts to meander and re-orient to the southeast (along the slope), as is finally estimated on Sep. 7 (Fig. 5d). This variation is hinted by the SST images (Fig. 4 and Section 7), but does not appear correlated to the atmospheric forcing which is weak during this period (see above). It is further evidence of the relatively important internal variability occurring along the Ionian slope.

4. Multivariate principal components and objective variability

"Objective" variability estimates are now exemplified. They agree with and complement the results of Section 3. They were computed by initialization (Section 4.1) and forecast (Section 4.2) of the dominant eigendecomposition of the (normalized) variability covariance matrix, for the Sep. 15–18 period. Since the initialization is challenging (an univariate 3D covariance is already too large to be easily stored), Section 4.1 starts with an outline of how this was carried out.

4.1. Initial variability subspace

A first-guess at the principal components of the (normalized) physical variability for Sep. 15 is computed based on Lermusiaux et al. (2000). Data and dynamics are combined in two stages: first,

---

Fig. 6. (a)–(d) Differences between HOPS SSTs shown on Figs. 4 and 5 (in °C, negative contours dashed): (a) Aug. 28 nowcast minus Aug. 22 nowcast, (b) Aug. 31 minus Aug. 28, (c) Sep. 04 minus Aug. 31 and (d) Sep. 07 forecast (Fig. 5d) minus Sep. 04 nowcast. (e)–(h) error standard deviations of HOPS nowcasts of SST, in °C (reflecting ship and aircraft tracks): (e) for Aug. 22 (Fig. 4c), (f) Aug. 28 (Fig. 5a), (g) for Aug. 31 (Fig. 5b), and (h) for Sep. 04 (Fig. 5c).

data and statistical fits to data are used to specify what is observed, the tracer (T and S) variability (Fig. 3), and then dynamical models are used to build and adjust what is not observed, the velocity variability.

4.1.1. First stage

The mesoscale tracer variability covariance is estimated, using the profiles at the stations shown in Fig. 3a and an approximate statistical model fit to these profiles. Briefly, the tracer covariance function is expanded into vertical functions, truncated to a unique spectral window (Nihoul and Djenidi, 1998), the mesoscale, and the result assumed separable in the horizontal and vertical (terrain-following or "sigma" levels). This simplification has been shown effective in other oceanic regions (e.g. Hua et al., 1986). In the vertical, the weighted multivariate EOFs of the mesoscale misfits between the tracer fields on Sep. 15 and the Aug. 12–Sep. 15 profiles (Fig. 3a) are computed directly. In the horizontal, the covariance is specified analytically and its parameters fit to data, leading to a decorrelation scale of 25 km[1] and zero-crossing of 50 km. The horizontal and vertical eigendecompositions are then combined using Kronecker product properties (Graham, 1981).

4.1.2. Second stage

To complete the physical variability subspace, the velocity variability adjusted to that of the tracers is computed by carrying out an ensemble of adjustment momentum integrations. The tracer variability covariance of the first stage is used to construct a set of perturbed initial tracer conditions. For each member of this set, the momentum equations are integrated forward, starting from the Sep. 15 velocity and perturbed tracer fields, keeping tracer fields fixed. These integrations modify velocities by tracer and velocity cross-covariances. They are carried out in parallel and stopped when the kinetic energy stabilizes and velocities are "PE adjusted" (i.e. all non-dimensional numbers, e.g. Rossby number, are then in the PE range). The size of the ensemble is increased until the number of differences between the unperturbed initial and PE adjusted fields is large enough for describing most of the mesoscale variability variance. This is assessed by a criterion which measures the convergence of the singular value decomposition (SVD) of the normalized differences (for each state variable, the norm is the volume and sample averaged variance, e.g. Lermusiaux and Robinson, 1999).

In the present procedure, the 3D tracer eigenvectors perturb the fields on Sep. 15 one at a time. The momentum equations are then integrated for 2 model days, starting from these perturbed fields, and keeping T and S fixed. Fig. 7 illustrates the differences between the PE adjusted fields and unperturbed initial conditions, for the four dominant tracer eigenvectors (Columns 1–4). Focusing on the first two rows of Fig. 7, the surface T and S patterns are in phase, with S partially compensating

---

[1] Mesoscale rings and eddies tend to have length-scales larger than the first Rossby radius of deformation R_d (e.g. Killworth, 1983; Killworth et al., 1997). Rings (large mesoscales, here subbasin scales) are usually larger and longer lived than eddies (smaller mesoscales). For the region considered here (Figs. 1–6), the order of R_d is 10 km (Artale et al., 1989; Robinson and Malanotte-Rizzoli, 1993). A decorrelation length fit to data at 25 km is thus adequate for the scales considered. It also agrees with previous mesoscale observations (e.g. Manzella et al., 1990).

T in density. This agrees with the dominant mesoscale variations of T and S observed above the main pycnocline: the T–S parity in the vertical is set up by the EOFs. The essential result is that these 3D tracer eigenvectors correspond overall to the dominant variations of the features independently revealed during the subjective analyses of the real-time fields (Section 3). Column 1 shows the first tracer eigenvector estimate and its associated velocity response; it is linked to the ABV. Column 2 shows the same, but for the second tracer eigenvector; it relates to the ISV. The third tracer eigenvector (Column 3) mainly identifies the MCC, coupling the two dominant vortices. Finally, the fourth tracer eigenvector (Column 4) has its largest amplitudes on the eastern side of Sicily. It is associated with the variability of the MRV, including its possible interactions with the ISV, as was suggested in Sections 3.2 and 3.3. The other 3D tracer eigenvectors explain smaller vertical or horizontal scales, depending on the eigenvectors entering the Kronecker product.

The 3D tracer eigenvectors are first-guess estimates, constructed using the in situ data and a simple covariance model. It is mainly the peculiarities of the Strait's geometry and tracer horizontal covariance function fit to data which lead to the relatively physics-related decomposition. Another factor is the choice of numerical domain, grid properties and data coverage (Section 2), which focus on the mesoscale dynamics near the southern and eastern coast of Sicily. In general, the eigenpatterns also depend on the orthogonality constraint, which can mask or spread dynamical processes. For example, on Fig. 7, the number of surface lobes increases with the vector number (the patterns of vectors 1 to q–1 influence those of vector q). The tracer eigenvectors are only an eigenbase: by definition, they estimate the orthogonal directions of the variability space associated with the largest normalized variance of T and S (a proxy for a non-dimensional potential energy). It is the aforementioned peculiarities that keep these directions almost aligned with the main features. The important point is that, all together, the dominant vectors support the group of features revealed in Section 3.

From the time-average view point, the patterns of the 3D vectors combine shifts in position and variations in strength, size and shape for all tracer features during Aug. 12–Sep. 15, as well as interactions among these features and with the background state. They aim to explain averages of variations (Figs. 6a–d), but not necessarily features. For example, the tendency on Figs. 6a–d most clearly explained by the four vectors is that of longest duration, averaging T variations over 8 d (Fig. 6a). Similarly, in relation to the northeastward motion of the ISV during Aug. 12–Sep. 15, the maximum on the second vector is around 36.8N, further north than the latitudes 36.4N to 36.6N of the ISV during Aug. 22–Sep. 7 (see Figs. 4 and 5).

The last two rows of Fig. 7 illustrate the flow responses (PE state variables ψ and $\hat{u}$, Section 2) to each of the above tracer components. They are clearly influenced by the local topography (e.g. Ionian slope along 16E to 17E) and by the fields on Sep. 15 (not shown). Within the Strait's basin, the sheared internal velocity often dominates the external velocity $\bar{\mathbf{u}}$ ($\mathcal{O}(\|\bar{\mathbf{u}}\|) \sim (\Delta\psi/L)/H$, where L is the local horizontal scale and H the local depth), e.g. see Columns 1 and 3. However, in the Ionian slope region, internal velocities only dominate in the upper layers (Columns 2 and 4); the amplitudes of the external velocity responses are there comparable to those of mid-depth and bottom internal velocities (2–10 cm/s, not shown). Focusing on ψ, since the first tracer vector (Column 1) perturbs the inflow boundary, there is logically a ψ response at the outflow (Ionian slope), indicating the effectiveness of the open-boundary condition scheme (Section 2). The
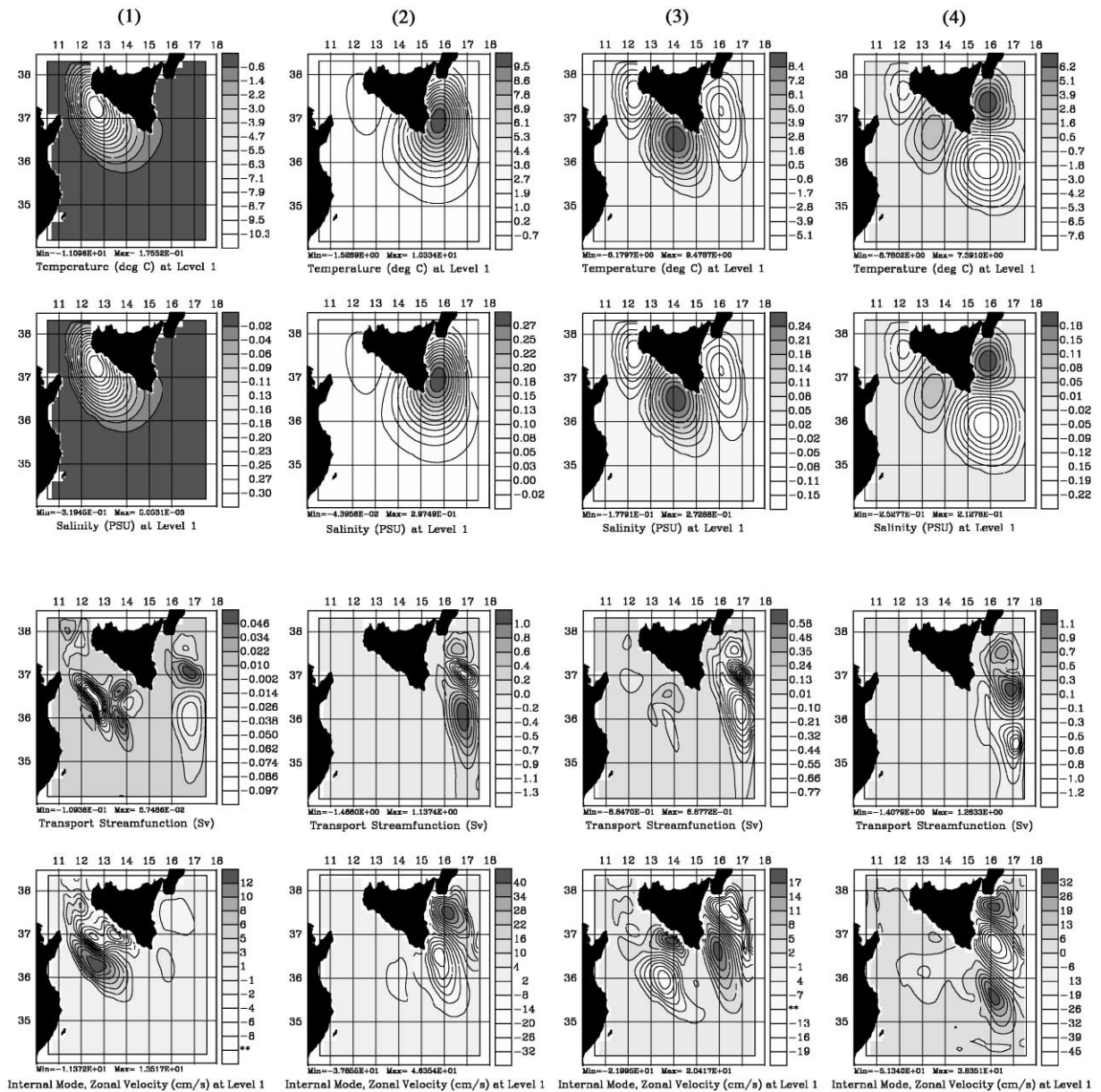
Fig. 7. Three-dimenional mesoscale tracer principal components number (1) to (4), and their "PE adjusted" velocity responses (the column numbers are the 3D tracer component numbers). Four fields are shown for each component; from top to bottom, the surface temperature and salinity perturbations, and the associated barotropic transport stream function and internal zonal velocity responses ($\hat{u}$ and $\hat{v}$ are close to geostrophic balance, hence only $\hat{u}$ is shown). All fields are dimensional.

locations and signs of the extremum horizontal gradient of ψ (i.e. large $\bar{\mathbf{u}}$) also vary with the perturbation: e.g. the velocity responses 3 and 4 are close to quadrature of phase above the Ionian slope.

4.1.3. Initial physical variability subspace

As the number of adjustment PE integrations increases, SVDs of the normalized differences of PE adjusted fields are computed and their convergence evaluated. After 289 integrations, the number of differences was found sufficient to represent the dominant variability. Fig. 8 illustrates the resulting first left singular vector. It mainly relates to baroclinic/barotropic topographic wave patterns along the steep Ionian slope. Looking at the ensemble of simulations (not shown), the vertically-averaged velocity patterns propagate along the slope[2] and are partly supported by subbasin-scale temperature and salinity slope fronts which, as we will find, arise as waters are exchanged between the Strait and Ionian basins (see Figs. 9–13 in Sections 4.2 and 5). The dominant horizontal wavelength is about 150 km (Fig. 8a), the time-scales range from the inertial period to several days (Section 4.2). In the upper layers, the non-dimensional total velocity anomalies dominate the tracer anomalies by a factor 3 to 10. This is in accord with findings in Section 3.3; in particular, such patterns are difficult to see from the SST alone. Vertical cross-sections along 17E are shown on Fig. 8b (large amplitudes are near 17E mainly because of the numerical slope, see Section 2). For the temperature, extrema are within 20–70 m, layer of dominant MAW variability along the slope. For the salinity, extrema are deeper, within 200 m to about 500 m, depths of the LIW core along the slope. Based on the magnitudes in the non-dimensional cross-sections (Fig. 8b), the main salinity effects on density anomalies are about 30–50% larger than the temperature effects. This indicates the importance of halocline variations at the Ionian slope (see Section 5). The internal velocity components along 17E (Fig. 8b) show a first baroclinic mode response, close to thermal-wind balance, with a zero-crossing around 300–500 m and a surface-intensified amplitude.

This first principal component is global and close to uniscale in the horizontal. In the ocean, the corresponding waves are likely localized and multiscale packets, induced in response to internal or atmospheric forcings, and interacting with the topography, mean flow and density fields. Several other principal components (not shown) are in fact necessary to explain most of the ensemble of adjusted differences: the first vector explains 3.5% of the physical variability accounted for by the 289 vectors, the dominant 5 vectors explain 15.6%. To represent most of the complexities near the Ionian slope, on various scales, the dominant 30 vectors are necessary. As a group, they explain 46.4% of the total variability accounted for in the numerical domain (Fig. 2). This "PE energy" percentage indicates that the subbasin-scale T and S fronts of the Ionian slope (see Sections 4.2 and 5) could have been chosen as features of dominant variability in the subjective evaluations (Section 3); they were not because they were not the main naval interest. The rest of the variability eigendecomposition on Sep. 15 is further described in Lermusiaux (1997, 1999b). Most vectors are associated with the ABV, MCC, ISV,

---

[2] Because tracers are fixed during one of such adjustments, the total (and internal) velocity responses mainly tend to thermal-wind equilibrium with the fixed T and S perturbations. The vertically averaged velocities, however, undergo a less constrained adjustment, as in Gill (1982). It is the SVD of the normalized differences of PE adjusted fields which can select physically adequate internal velocity and tracer anomalies.

(a)   **(b)**

Temperature at Level 1

Salinity at Level 1

Internal Mode, Zonal Velocity at Level 1

Transport Streamfunction

Temperature

Salinity

Internal Mode, Zonal Velocity

Internal Mode, Meridional Velocity
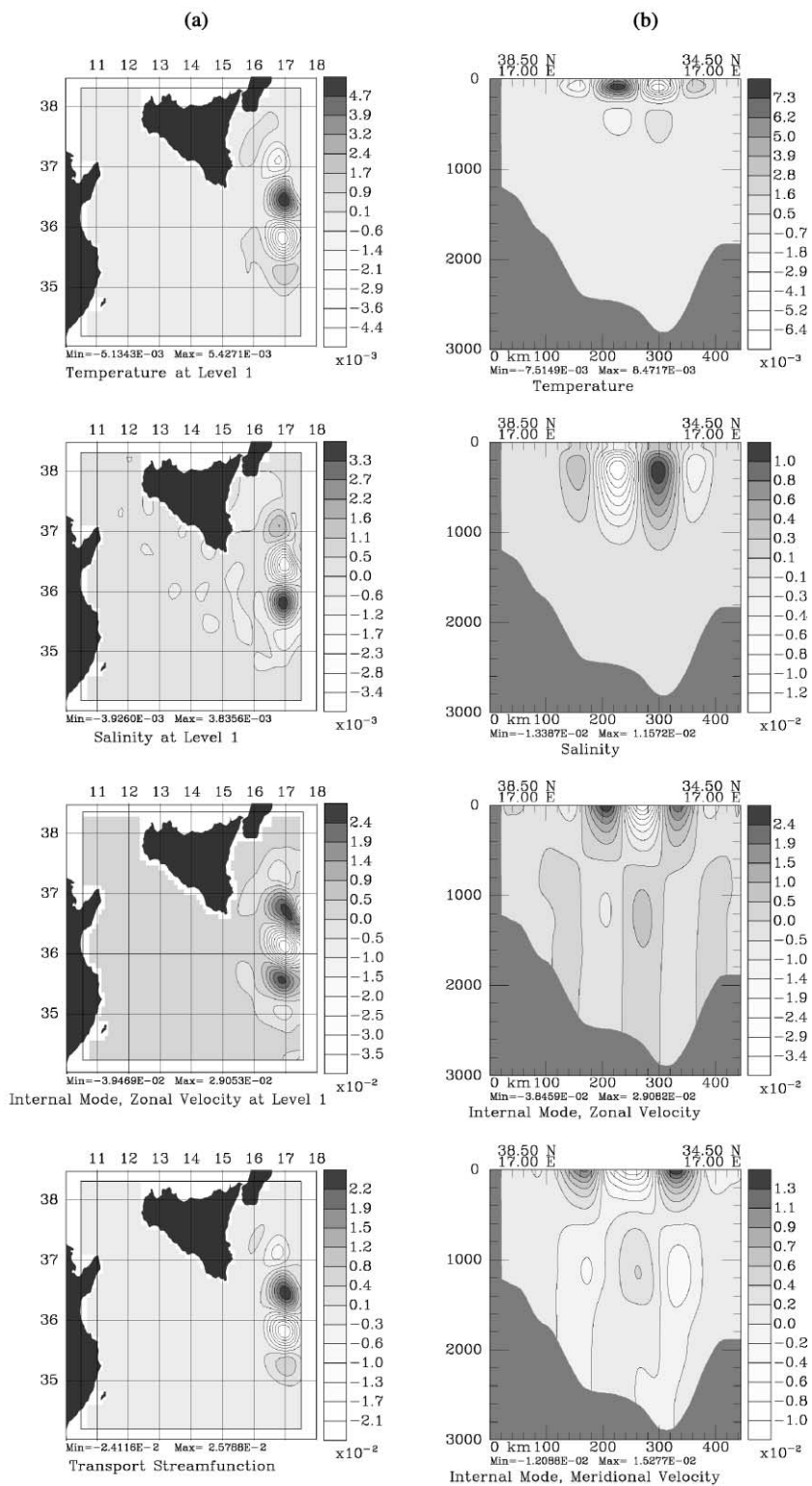
MRV and Ionian slope region. They are more complex than on Fig. 7, mainly because of the multivariate dynamics and multiscale interactions, but also because of the orthogonality constraint.

4.2. Variability forecast example

4.2.1. Variability covariance on Sep. 18

To account for nonlinearities, the dominant variability is forecast by an ensemble of Monte-Carlo PE forecasts. The PE fields on Sep. 15 are first perturbed using a zero-mean, random combination of the variability principal components for Sep. 15 (Section 4.1). For each of these perturbed initial conditions, the PE model is integrated until the forecast date, Sep. 18. These Monte-Carlo integrations are carried out in parallel until the size of the ensemble is large enough to describe most of the variability for Sep. 18. This is assessed by measuring the convergence of the SVD of the ensemble of normalized forecast differences (Lermusiaux, 1997), which was achieved here after 285 differences.

One of such forecast differences for Sep. 18 is illustrated in Fig. 9a. It is representative of complex variations that can occur along the Ionian slope. East of 15E, local wave-like patterns, with a succession of highs and lows in the tracer and velocity fields, are superposed on frontal meanders and corresponding currents (e.g. see north–south elongated T, S and ψ variations). The first initial eigenvector (Fig. 8) estimated the dominant component of such patterns for Aug. 12–Sep. 15. Of course, within the ensemble of forecast differences, some are simpler than on Fig. 9a, being either more wave-like or more meander-like, while some do not have their largest amplitudes along the Ionian slope at all.

Fig. 9b illustrates the forecast of variability standard deviations (square-roots of the diagonal elements of the covariance matrix), based on the ensemble of 285 differences. On Sep. 18, the ABV, MCC and Ionian slope processes dominate the surface variability; the ISV and MRV are much less variable. Along the slope, a new result is that the largest temperature variability is located from about 36N to 38N (main AIS path in summer) and the largest salinity variability from 34.5N to 36.75N (boundary between the Strait and Ionian water masses, and main LIW path). The corresponding subbasin-scale T and S slope fronts thus dominate at different locations (and different depths, e.g. Fig. 10b hereafter). The overlap, from about 36N to 36.75N, has been referred to as the Maltese shelfbreak front (Briscoe et al., 1974; Lavenia and Pisani, 1974). As was observed in 1994 (Robinson et al., 1999), the upper layers of this Maltese front are simply a portion of the AIS frontal system, mainly the eastern side of the ISV. Focusing on the vertically averaged transport, around Sep. 18, the standard deviations of ψ through the Strait are estimated to be in the 0.1–0.2 Sv range, while they are about 1 Sv along the Ionian slope. The dominant eigenvectors of

Fig. 8. First eigenvector of the (normalized) initial PE variability covariance estimate for Sep. 15. All variables are non-dimensional. Column (a): surface values; Column (b): vertical cross-section along 17E. The size of the complete covariance matrix would be [299,052 × 299,052]. For each variable, the norm is the volume and sample averaged variance. This involves a division by the total number for samples, hence the leading order of 10^{-2} for all variables.
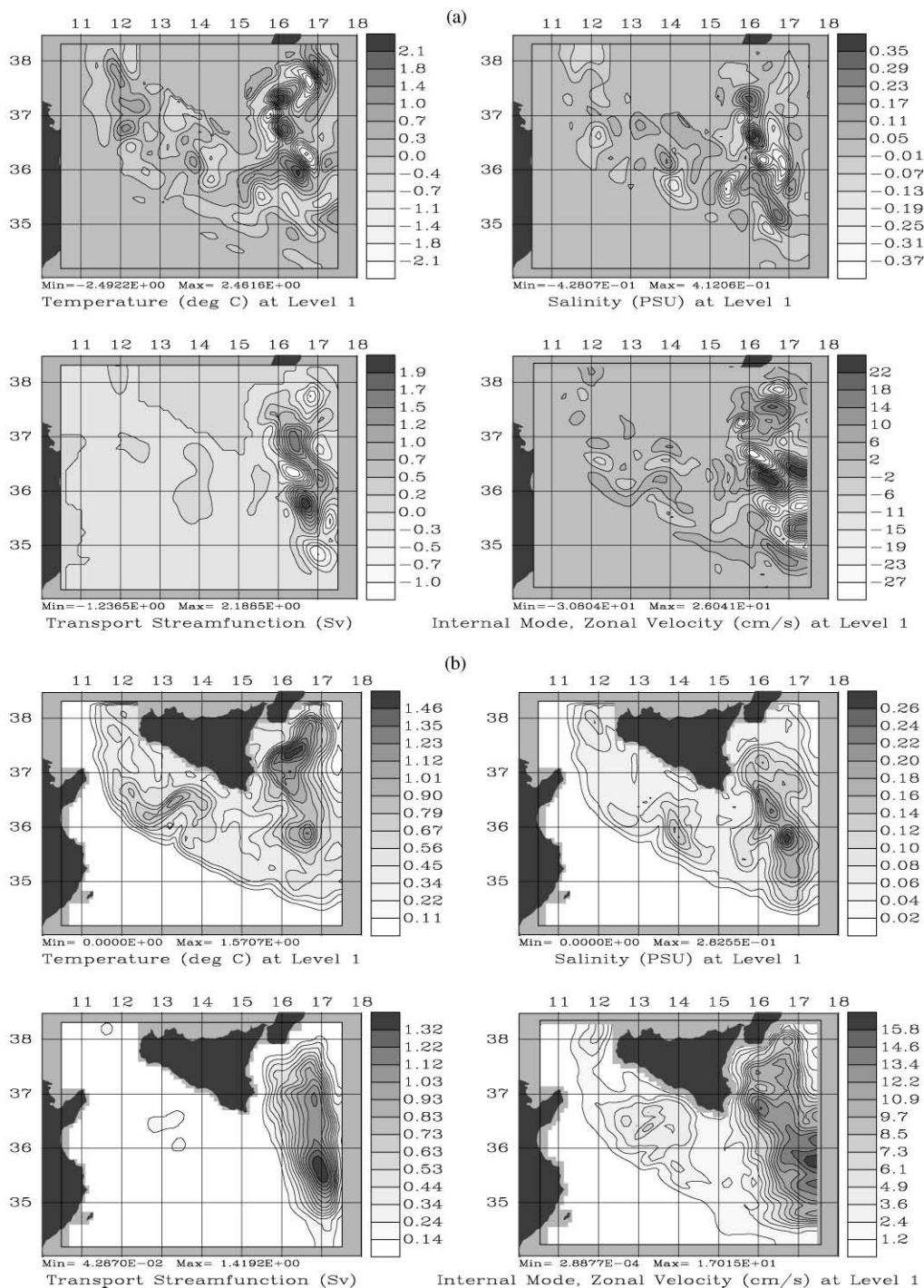
Fig. 9. (a) Represents a sample snapshot of variability, as forecast for Sep. 18. It shows differences between surface fields of two 3-day PE forecasts for Sep. 18 which have initial conditions differing in accord with the variablity covariance estimate for Sep. 15. (b) Variability standard deviations forecast for Sep. 18, computed by a Monte-Carlo approach (ESSE) that creates sample forecasts and increases significance up to a certain convergence limit.

the physical variability covariance forecast for Sep. 18 (not shown) contain similar patterns as these of Sep. 15 (e.g. Fig. 8), but with the above temperature and salinity peculiarities. Their evolution and the use of variability forecasts for the design of sampling strategies are discussed in Lermusiaux (1997, 1999b).

4.2.2. Characteristic scales of state variables and their variability

Combining the PE fields (see Figs. 4–6 above, also Fig. 10) with the variability standard deviations exemplified by Fig. 9b, the surface horizontal T and S characteristic scales are of the order of: $\Delta T = 4 \pm 1\,^\circ\text{C}$ and $\Delta S = 0.4 \pm 0.1\,\text{PSU}$ (usually opposite) for the AIS and MCC, $\Delta T = 2 \pm 0.5\,^\circ\text{C}$ and $\Delta S = 0.25 \pm 0.05\,\text{PSU}$ for the vortices (ABV, ISV and MRV), $\Delta T = 4 \pm 1\,^\circ\text{C}$ for the Ionian T front and $\Delta S = 0.6 \pm 0.2\,\text{PSU}$ for the Ionian S front. The amplitudes of the surface currents and vertically averaged transport are: for the AIS and MCC, $\|\mathbf{u}\| = 35 \pm 15\,\text{cm/s}$ and $\Delta\psi = 1 \pm 0.2\,\text{Sv}$, for the ABV, ISV and MRV, $\|\mathbf{u}\| = 15 \pm 5\,\text{cm/s}$ and $\Delta\psi = 0.4 \pm 0.1\,\text{Sv}$, and for the Ionian slope fronts, $\|\mathbf{u}\| = 20 \pm 15\,\text{cm/s}$ and $\Delta\psi = 3.5 \pm 1\,\text{Sv}$. Obtaining $\Delta\psi$ estimates has been historically difficult (e.g. Manzella et al., 1988; Moretti et al., 1993; Astraldi et al., 1999); the advantage here is that each $\Delta\psi$ and its standard deviation has been estimated by assimilating real data in the PE dynamics.

5. Circulation patterns, water pathways and hydrographic features

Guided by the above results, we examine the circulation patterns and water pathways at key locations and on characteristic potential density anomaly iso-surfaces ("σ_θ surfaces"). Based on the initial (Section 4.1) and forecast (Section 4.2) variability estimates, specific attention is given to processes and features related to the Ionian slope.

5.1. Circulation patterns and water pathways at selected locations

5.1.1. Surface and depth-averaged circulations

The surface fields for Sep. 18 (Fig. 10a) confirm the meanders of the AIS, especially the total velocity map. The cyclonic ABV, ISV and MRV, and anticyclonic MCC, are easily seen on the surface temperature and salinity. In the ψ field, the three vortices correspond to lows and the MCC to a high. These features are in accord with the successive stretching and squeezing of the AIS, which can thus conserve potential vorticity as it flows over topography (Fig. 2), as Onken and Sellschopp (1998) also inferred. The advection of MAW is noticeable, with lower surface salinities (less than 37.4) all along the meanders of the AIS, as reported by Moretti et al. (1993). At about 16E, the AIS reaches the Ionian slope and bifurcates, here with a strong branch going north and a weaker one going south–southeast along the slope. A substantial mesoscale activity (eddies, meanders, etc, e.g. see T and S maps) is estimated more or less within 15E and 17E; this strip and its width relate to mesoscale variations surrounding the slope. The barotropic transport through the Strait is estimated to be about 1 Sv, eastward. Along the curve of the Ionian slope, the barotropic current is northward, adding to about 3–4 Sv.
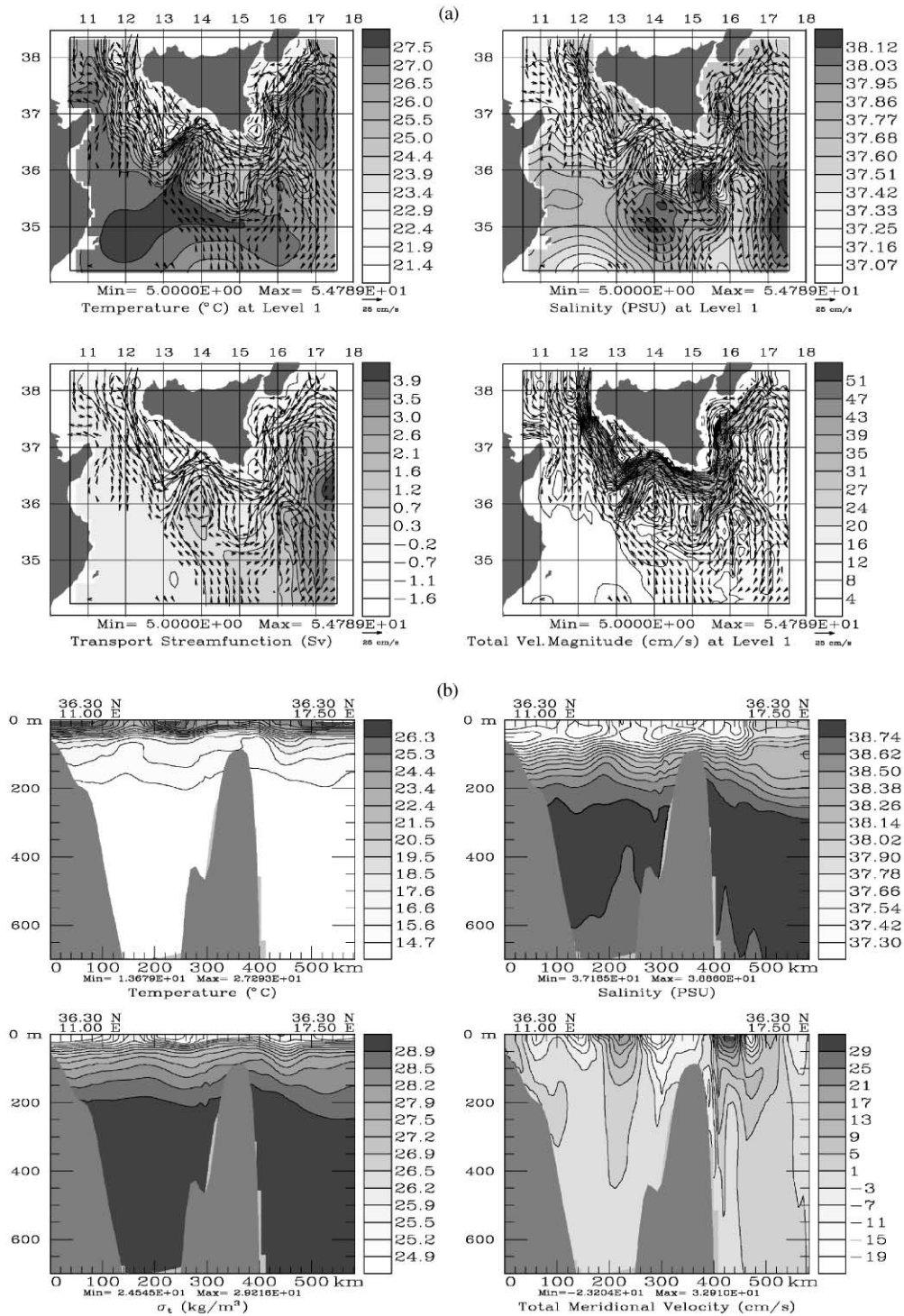
Fig. 10. PE field forecast for Sep. 18, 1996. (a) Surface fields, overlaid with surface velocity vectors when the velocity is larger than 5 cm/s (scale arrow is 25 cm/s). (b) Cross-sections along 36.3E, from the surface down to 700 m. The topography is the raw etopo5 data.

5.1.2. Depth-dependent circulation and Ionian slope fronts across the "Maltese front"

In cross-sections along 36.3N (Fig. 10b), in the upper isopycnals (see upper-layer stratified T and density anomaly σ_t), the tip of the ABV dome, tip of the MCC trough and most of the ISV dome are visible. The corresponding normal velocities (v on Fig. 10b) are close to thermal-wind balance and strongly influenced by topography (e.g. see reversal of the mean flow above the Maltese plateau). The S and σ_t sections show: (i) the inflow of MAW from west to east in the upper 100 m, up to the Ionian slope area at about 16E; and (ii), the outflow of LIW from east to west at mid-depth, in the Strait's basin from 250 m to about 500 m. Interestingly, these S and σ_t sections reveal that the core LIW does not pass above the Maltese plateau, but goes around it, south of Malta (Fig. 2).

On the Ionian slope (near 15.8–16.2E at 36.3N), in the upper 100 m, the MAW and IW form a front (an across-slope, horizontal density gradient) which is T dominated from about 20 to 70 m. The S gradient (fresh MAW and salty IW) is opposite to that of T at these depths but is not dominant and only reduces the thermal wind. Below the MAW, the upper layers of the LIW are rising with the Ionian slope (but without passing above the plateau). This rise leads to a sub-surface "front" within 15.6–16.4E, from about 100 to 500 m in depth. At this location, T and S combine positively on the density gradient, but S now dominates by 30–50%. Considering the complete 0–500 m water column, the upper-layer T-dominated front and subsurface S-dominated front add effects (see σ_t on Fig. 10b). They locally explain the mean northward flow along the curved Ionian slope (Fig. 10a) since this flow is close to geostrophic equilibrium within 0–500 m (see positive v on Fig. 10b). These results are in quantitative agreement with the properties of the variability revealed in Section 4.1 (e.g. Fig. 8).

5.2. Main water masses, their pathways and transformations

To study the pathways and transformations of the three main water masses (MAW, IW and LIW, see Section 2), we used the PE fields and computed, for several days, the salinity, temperature, depth and horizontal velocity on 20 σ_θ surfaces. For each water mass, we then selected a representative σ_θ value. The corresponding fields (Figs. 11–13) are now described, focusing on Sep. 18 so as to continue the chronological order (Sections 3 and 4), and have assimilated all data.

5.2.1. MAW paths

From the four fields shown on the $\sigma_\theta = 27.5$ surface (Figs. 11a–d), the low salinities of the core MAW are along the AIS path, including the offshore edges of the cyclonic vortices (ABV, ISV and MRV) and MCC. At the Ionian slope, where the AIS bifurcates, most of the MAW is advected northward in the main branch of the AIS. The other branch, flowing south–southeast around Sep. 18, is weak on the $\sigma_\theta = 27.5$; at these depths (Fig. 11b), this branch advects less MAW than at the surface (Fig. 10a). In accord with the August observations (Figs. 4 and 5) and surface drifter data (see Section 6), there is not much core MAW along the Tunisian shelf. During the present stratified period, most of the MAW is entrained by the main AIS and remains near the Sicilian coast (Section 3.1).

The ranges of salinity (37.25–37.6 PSU), temperature (16–17°C, not shown) and depth (40–70 m) of the core MAW on this σ_θ are within the ranges identified on the T/S diagram (Fig. 3b) and
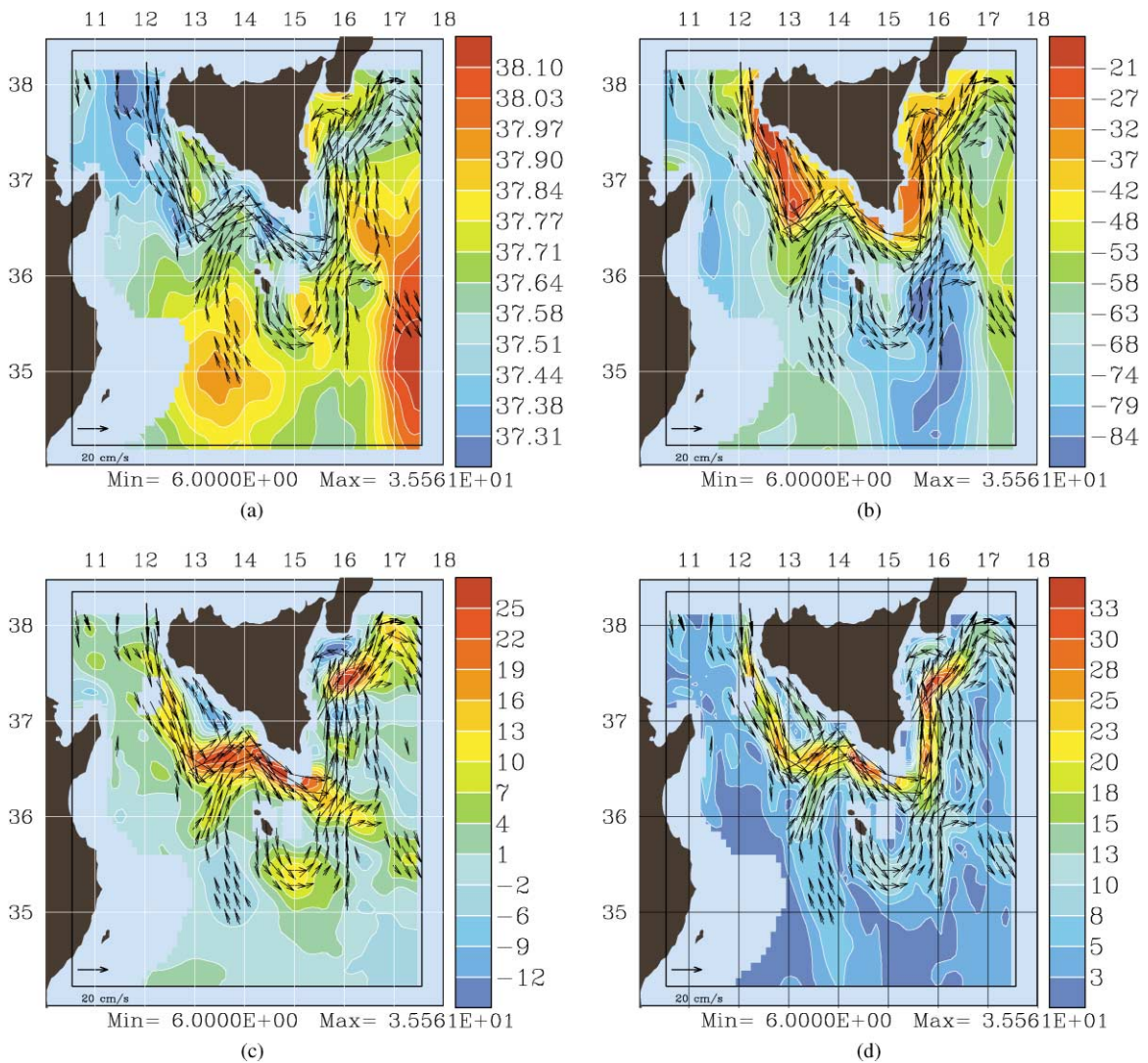
Fig. 11. Core MAW paths. (a) Salinity, (b) depth (m), (c) zonal horizontal velocity (u, cm/s), and (d) total horizontal velocity magnitude ($\|\mathbf{u}\|$, cm/s), on the surface $\sigma_\theta = 27.5\,(\text{kg/m}^3)$ for Sep. 18. The four fields are overlaid with total horizontal velocity vectors, again on $\sigma_\theta = 27.5$ (scale arrow is 20 cm/s). These velocity vectors are only plotted every two grid points, if $\|\mathbf{u}\|$ is larger than 6 cm/s (the min and max below each plot are for $\|\mathbf{u}\|$ plots).

The raw topography (etopo5) and positions for which the density $\sigma_\theta = 27.5$ is not found in the water column are plotted in gray. Note that the number of "sea" grid points for velocity can be smaller than for tracers because of the staggered topographies and grids; this explains the usually wider gray zones on the u and $\|\mathbf{u}\|$ plots.

variability estimates (Section 4). Along the main AIS path (Fig. 11b), the core MAW is advected on this σ_θ at speeds within 15–30 cm/s (Fig. 11d). For a parcel remaining in this core (without being trapped in eddies, etc.), the corresponding residence time from (38N, 12E) to (38N, 17.5E) is about
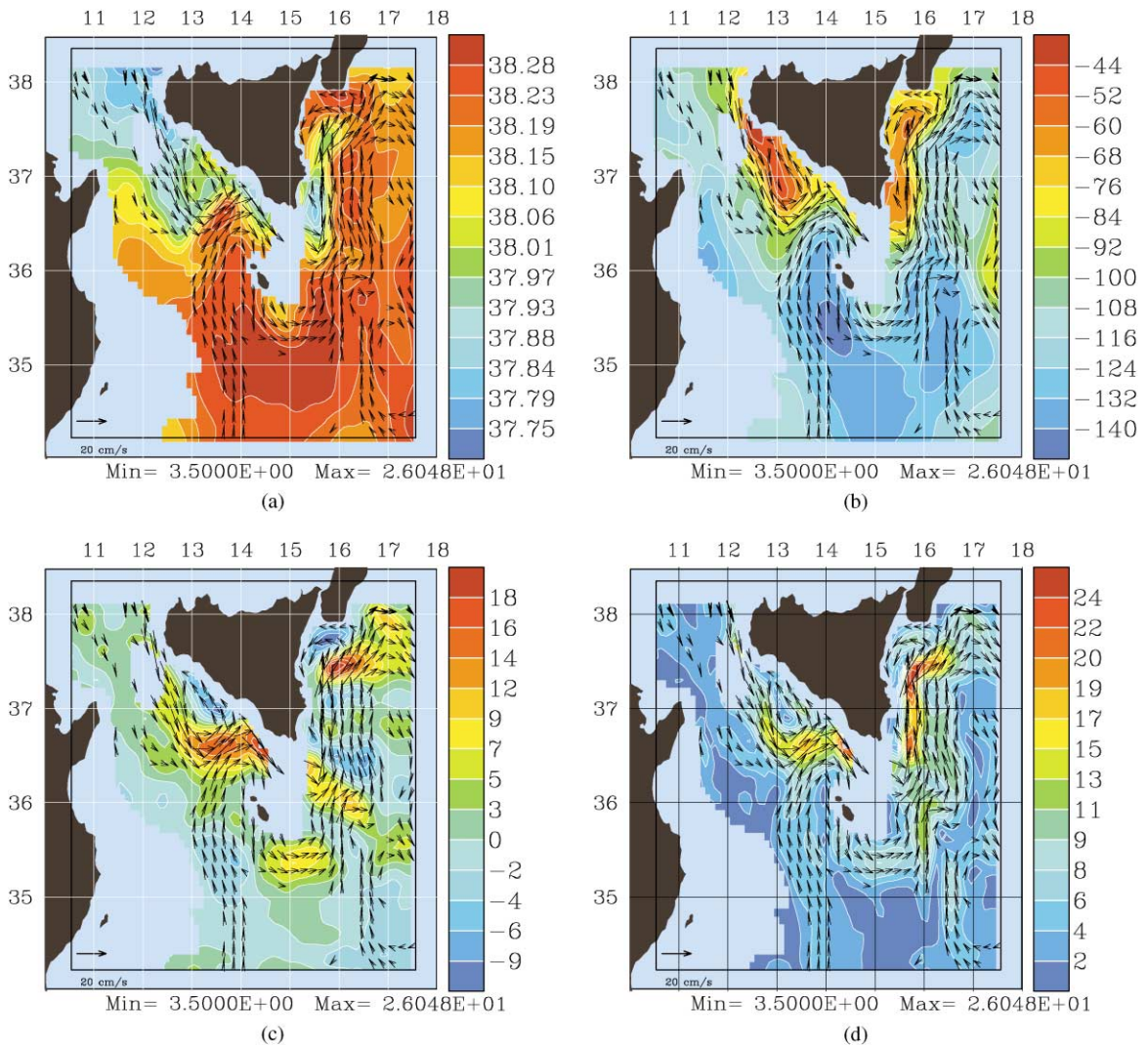
Fig. 12. Core IW paths: as for Fig. 11, but for $\sigma_\theta = 28.25$ and with velocity vectors plotted if $\|\mathbf{u}\|$ on $\sigma_\theta = 28.25$ is larger than 3.5 cm/s. All other conventions are as on Fig. 11.

30–60 d. Along this path, the MAW is transformed by atmospheric forcing and internal mixing (e.g. with the IW): for example, S increases from 37.25 to 37.5 PSU, in accord with older data (e.g. Malanotte-Rizzoli et al., 1997; Warn-Varnas et al., 1999).

West of the Ionian shelfbreak, the largest horizontal PE velocities (Fig. 11d) are often along the steepest slopes of the depth of the σ_θ surface, with the shallowest depths on the left (Fig. 11b). This property also holds for the IW and LIW (see Figs. 12b and 13b). Over most of the Strait's basin, fields are thus close to thermal-wind balance. However, east of the Ionian shelfbreak (above and

past the Ionian slope), this is less true, in agreement with our variability estimates (Section 4 and Lermusiaux, 1999b).

5.2.2. IW paths

For $\sigma_\theta = 28.25$ (Fig. 12), the most striking field is the salinity (Fig. 12a). In the Ionian and south of the AIS inside the Strait's basin, it is almost uniform, within 38.1 and 38.3 PSU (T within 15.5°C and 16.2°C). These values clearly correspond to the core IW identified on Fig. 3b. The depth-range, about 90–145 m (Fig. 12b), also corresponds.

The horizontal velocity and depth on this $\sigma_\theta = 28.25$ (Figs. 12b–d) reveal that the core IW has two pathways. One enters our domain near (34.5N, 17E) and follows the Ionian slope, interacting with several eddies and forming weak branches as it progresses northward to the east of Calabria. The other starts at (34.5N, 14E) and follows the Tunisian shelf, with a speed of about 5 cm/s. Southwest of Malta, this broad pathway bifurcates. The first branch veers east, flows south of Malta and then follows the Ionian slope northward, joining the first pathway. The second branch continues north, reaches the MCC, is then entrained to the east and finally rises above the Maltese plateau within the AIS, mixing with MAW along the way.

A tongue of warm water over the central region of the Strait had been observed in winter from surface data, but its precise origin was unknown (Grancini and Michelato, 1987; Manzella et al., 1990). The fields on Fig. 12 reveal that the main IW pathway creates this warm and salty tongue. In winter, under the reduced stratification and increased vertical mixing, the tongue can be visible on the SST. The fields on Fig. 12 also indicate that, in summer, the IW enters the Strait but does not easily flow in the western Mediterranean; it can be blocked by the energetic AIS and its MAW. On Sep. 18, the only IW overflow is via a thin and sluggish 1–3 cm/s current along the Tunisian shelfbreak within 110–130 m depths (Figs. 12c–d).

5.2.3. LIW paths

From the fields on the $\sigma_\theta = 29.05$ surface (Fig. 13), by large-scale thermohaline forcing, the LIW slowly rises above the Ionian slope (as far south as about 34N), enters the Strait's basin and then flows into the western Mediterranean. East of the Ionian shelfbreak, the rising is clear (Figs. 13a and b). While the depth on the $\sigma_\theta = 29.05$ rises from about 350 to 275 m around Medina Bank (Fig. 2) and from 350 m to a depth below that of the shelfbreak elsewhere (160–200 m), the salinity and temperature remain relatively uniform, within 38.75–38.82 and 14.2–14.4°C (not shown). Haloclines are squeezed, and, by thermal wind, a mean northward flow builds along the curved Ionian slope (see Fig. 13d for $\|\mathbf{u}\|$ and Fig. 10a above for ψ). A portion of the LIW thus flows north without entering the Strait and possibly re-circulates in the Ionian Sea. During RR96, the main passage of LIW above the Ionian shelfbreak is found to be through the two sills bordering Medina Bank; around Sep. 18, it is mainly through the southern sill (Figs. 13a–c). Note that from in situ data alone, this expected sluggish westward motion of LIW has been difficult to outline in the region (e.g. Grancini and Michelato, 1987): combining data with realistic dynamics is essential.

Inside the Strait's basin, the main westward flow of LIW is along the Tunisian slope, within depths of 220–270 m (Figs. 13a and b) and horizontal speeds of 1–3 cm/s (Figs. 13c and d), leading to a minimum residence time of 150 – 450 d. However, under the influence of both topographic and density features, some of the LIW (re)-circulates in the basin. For example, in between the
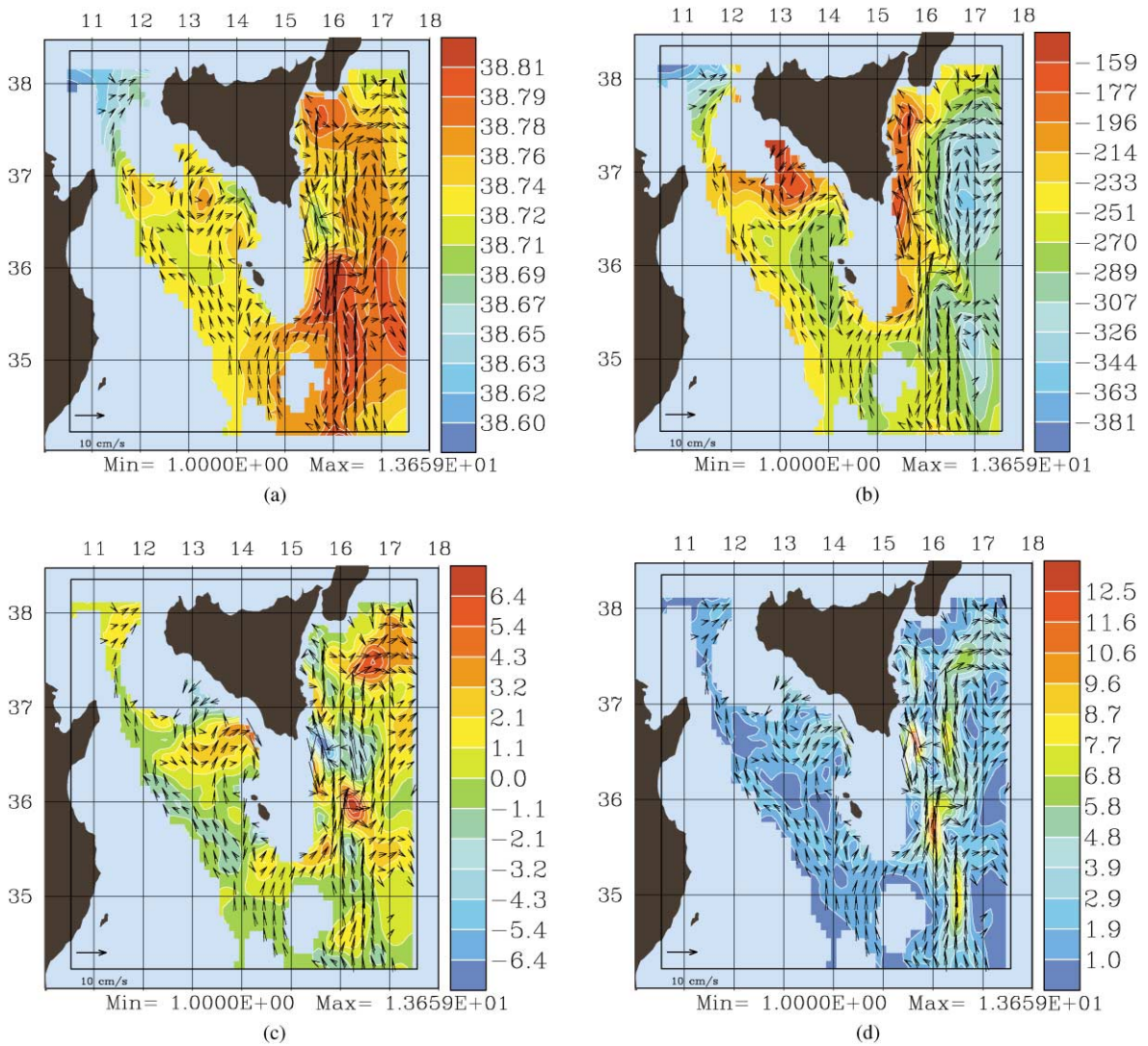
Fig. 13. Core LIW paths: as for Fig. 11, but for $\sigma_\theta = 29.05$. The scale arrow for velocity was re-scaled down to 10 cm/s. The minimum $\|\mathbf{u}\|$ to be reached on this $\sigma_\theta = 29.05$ before a velocity vector is plotted was also reduced to 1 cm/s. All other conventions are as on Fig. 11.

Adventure Bank and Maltese plateau, there is a pair of lenses (subsurface eddies), one cyclonic, one anticyclonic. They are separated by the bottom of the MCC, and the anticyclonic lens is above a 750 m deep trough (Fig. 2).

On top of the main western sill, the overflow is northward, of horizontal velocities near 1 cm/s. This speed at the sill varies with time: e.g. on Sep. 5, it is estimated to reach about 4 cm/s (not shown). Even though such variations are in accord with coherent pulses of LIW (Astraldi et al.,

1999), the number of CTDs (Fig. 3) and of grid points at the sill are not large enough in our simulations to confirm the pulses. Once the LIW enters the Tyrrenian Sea (Fig. 2), being denser than Tyrrenian waters at the overflow depth, it sinks as the topography deepens (in our domain, from 250 to 400 m on $\sigma_\theta = 29.05$, Fig. 13b). The sinking creates an horizontal density gradient and a mean southwestward thermal wind. Nonetheless, near Sep. 18, the main flow is opposite (see Figs. 13c and d): the LIW turns north-eastward as it exits the Strait, with horizontal speeds reaching 1–3 cm/s along the Sicilian slope. This is because the topographic constraint and Coriolis veering dominate the thermal wind effect. This result agrees with the idealized studies of Herbaut et al. (1998) and recent observations of Astraldi et al. (1999) and Sparnocchia et al. (1999). The mechanism differs from that creating the northward flow of LIW along the Ionian slope since there, the thermal wind, relief and Coriolis effects combine positively (see above results).

As reported in (Moretti et al., 1993; Manzella et al., 1988; Astraldi et al., 1999), the LIW fills most of the $\sigma_\theta = 29.05$ surface, indicating a broad overflow from the Ionian Sea (Figs. 13a and b). This contrasts with the localized flow of MAW in the upper layers (Fig. 11). However, substantial mixing of LIW occurs (Warn-Varnas et al., 1999). We find here that this mixing mainly happens above the two sills of the Strait and in lenses within the Strait's basin (see Figs. 13a and b). Going up and down the sills, the shear and vertical motions are large, and turbulent mixing is thus intense: passing over the Ionian shelfbreak, the LIW salinity decays by about 0.08 PSU (T by 0.2°C), over the Tyrrenian shelfbreak (steeper sides), by about 0.1 PSU (T by 0.25°C). Inside the Strait's basin, geostrophic turbulent mixing occurs in lenses and other mesoscale features, but it is less efficient (see Fig. 13a).

5.2.4. Main characteristic T/S regions

Guided by the above results, we separated the CTD profiles (Fig. 3b) into five regions (Fig. 14a). The clear outcome shows again how data assimilative models can help the study of in situ data. The water masses contained in the profiles of region 1 (west of Strait, Fig. 14b) are mainly: surface MAW, core MAW and LIW, combining in a "crescent" shape. There is not much IW, which agrees with Figs. 12 and 13. In region 2 (northern Strait, Fig. 14c), the surface and core MAW become warmer and saltier by atmospheric forcing and mixing, as indicated in interpreting Fig. 11. There is some IW in the profiles south of the MCC (as on Fig. 12). In between the Adventure Bank and Maltese plateau, there is some LIW and some transition waters to LIW. Region 3 (southern Strait, Fig. 14d) contains most of the salty and warm SIW, and core IW, of the Strait. Mixing between these waters and the MAW is visible. The "IW-to-LIW" transition waters are also clear; this Region 3 contains most of the LIW of the Strait's basin, in accord with Fig. 13. Overall, the "staircase" shape representative of summer western Ionian waters is visible (compare with Fig. 14f). The hook towards EMDW is still weak, indicating that the EMDW has either not penetrated significantly in the Strait's basin or has already been mixed with the LIW, e.g. geostrophic mixing in subsurface lenses (Fig. 13). Because of the AIS advection, Region 4 (Ionian slope and eastern Sicilian shelf, Fig. 14e) contains most of the surface MAW and core MAW that flows in the Ionian Sea (Figs. 10–13). There is however not much IW (no staircase shape): one has to cross the Ionian slope T front and enter Region 5 to find the SIW and IW. Below the LIW, there are transition waters towards both EMDW and ADW (ADW that mixes with LIW and EMDW as it outflows the Adriatic Sea, e.g. Malanotte-Rizzoli et al., 1997). In Region 5 (Ionian Sea, Fig. 14f),
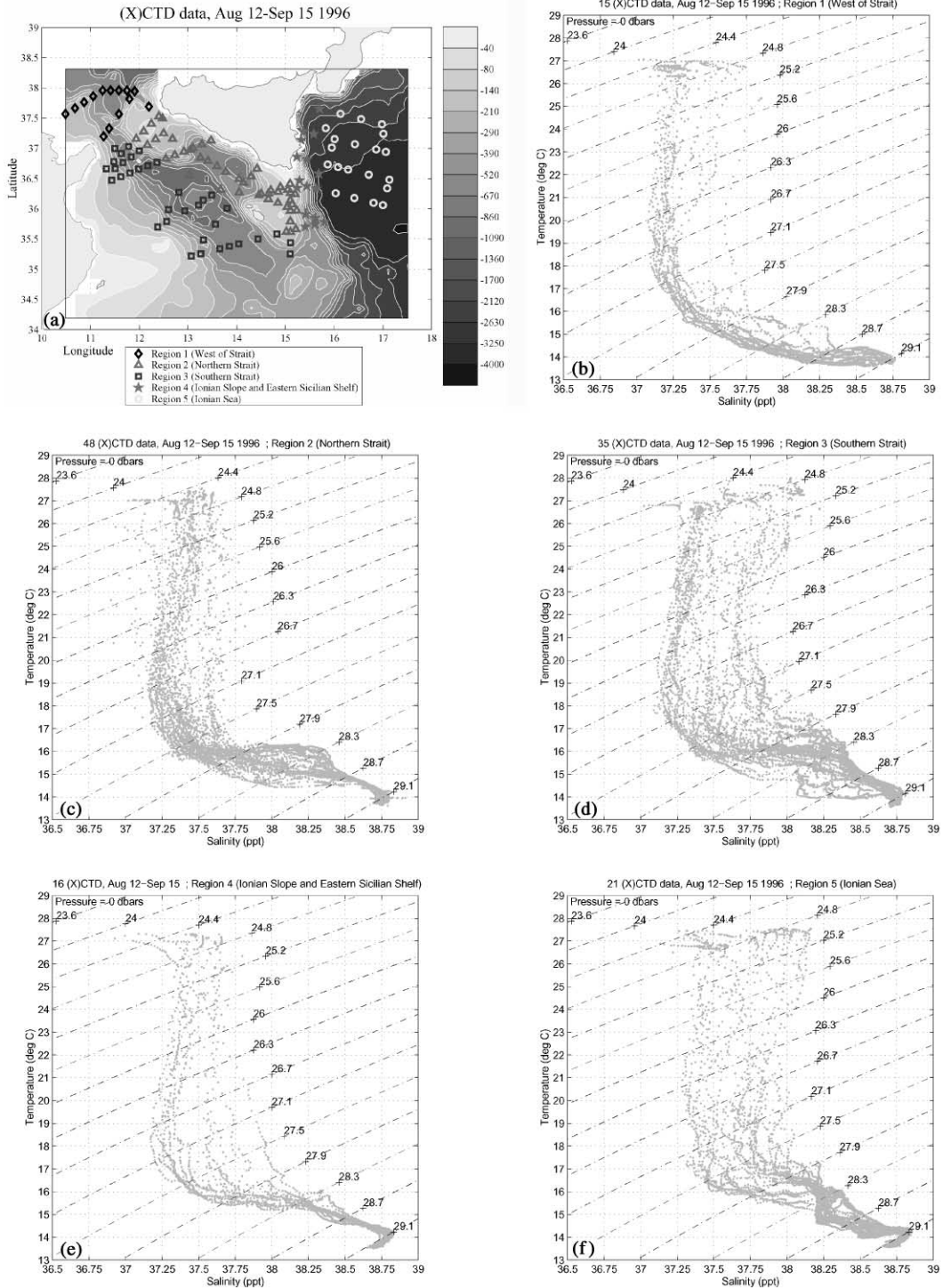
Fig. 14. *T/S* diagram of the CTD data (b)–(f), separated in 5 characteristic regions (a).

there is not much surface MAW and core MAW. The staircase shape dominates, with mainly SIW, IW, LIW and the hook towards EMDW. As shown on Fig. 13, the LIW becomes cooler, fresher and slightly lighter as it mixes and spreads westward: Regions 5 and 4 contain the saltiest and warmest LIW, Region 1 the freshest and coldest.

5.3. Ionian slope fronts and associated wave patterns

The structures of the Ionian slope fronts (ISFs) at latitudes other than those of the "Maltese front" (Section 5.1, Fig. 10b) are found in accord with our variability estimates (Section 4.2, Fig. 9b). North of 36.3N, the T and S fronts are both present. Along the Messina Rise and Calabria, the upper-layer front is maintained by the AIS and its MAW (Figs. 10a, 11 and 14e). At mid-depth, by inertia of the western boundary flow of LIW (Fig. 13d), isopycnals still slope upward, with S dominating (Figs. 13a and b). Overall, the two fronts combine into an upper-ocean current, the northern branch of the AIS. However, south of 36.3N (south of the ISV and Malta), there is essentially only the subsurface LIW front. This is because, in the upper layers, southern Strait waters are on average warmer and saltier than northern Strait waters (Figs. 10a, 11, 12 and 14c–d) and are therefore closer to Ionian waters. The upper-layer horizontal density gradient is thus weak (on Sep. 18, it is in fact slightly opposite to that at mid-depth, compare Fig. 11b with Figs. 12b and 13b). At mid-depth, the LIW front leads to a mean northward flow (Figs. 13). This S dominated, horizontal density gradient is analogous to that of Fig. 10b, but its depth range and strength vary with the local topography of the Ionian shelfbreak (Fig. 13b).

An important result is that the fields on the σ_θ's strengthen the findings of the variability principal components (Section 4): the steep Ionian slope, and its temperature and salinity fronts, can support topographic wave patterns. On the zonal velocity fields of Figs. 11c, 12c and 13c, there is a succession of positive and negative lobes along the intersections of the σ_θ surfaces with the slope. Once at LIW depths, such lobes are along the whole slope (Fig. 13c). The salinity and depth on the σ_θ's also contain a substantial number of highs and lows along the slope (meanders, weak eddies or lenses), especially at LIW depths where the surface dynamics are less influent (Figs. 13a and b). Total velocities clearly show a succession of convergence and divergence zones (highs and lows on Fig. 13d). For all of these variables, the dominant wavelengths (150 ± 50 km) and depths (Figs. 11b, 12b and 13b) are similar to these estimated on Fig. 8.

Since most of such waves propagate in a southward direction while the mean, buoyancy-driven, slope current is to the north (Figs. 11–13), there is a possibility for quasi-stationary wave packets (e.g. Pedlosky, 1987). For a complete characterization, additional in situ data and idealized studies will be helpful. For example, based on an idealized adjustment of the abyssal eastern Mediterranean, Curchister et al. (1999) have reported the importance of Kelvin and Rossby waves, and of a western boundary current, along the abyssal Ionian slope.

6. Features and variability from drifter data

On the basis of the results of Sections 3–5, we searched for independent data to further corroborate the features and variabilities found. Fig. 15 shows the trajectories of surface drifters
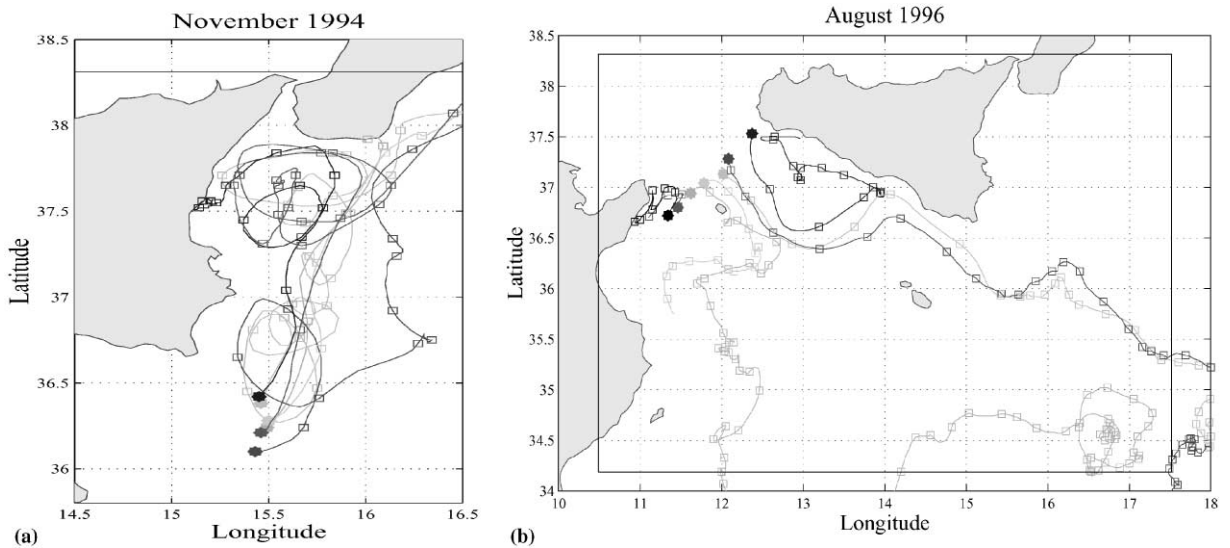
Fig. 15. Surface drifter trajectories (data provided by Prof. Pierre-Marie Poulain). (a) Six drifters released near the Ionian shelfbreak (near 15.5E) on Nov. 21, 1994. (b) Seven drifters released at the western entrance of the Strait between 18:00GMT Aug. 13 and 18:00GMT Aug.14, 1996. The stars indicate the deployment sites. For each trajectory, every two days starting from the deployment time, a square is drawn. The numerical model domain is shown as a solid line/contour. On Panel (b), the 2-day interval between squares (starting on Aug. 13–14) can be used to further verify the surface HOPS estimates (Figs. 4–5 and 9). This evaluation is briefly described in the text.

(Sellschopp and Robinson, 1997; Robinson et al., 1999) released in the vicinity of the Ionian shelfbreak in 1994 (Fig. 15a) and in a section crossing the Adventure Bank in 1996 (Fig. 15b). The drifters used were modified CODE designs (Poulain, 1999, 2001) extending within the first meter of water. They follow surface waters with 2–3 cm/s accuracy even in relatively strong wind conditions. The trajectories (Fig. 15) confirm the ABV, MCC, ISV and MRV as dominant features in the region. In fact, the first drifter set in the ISV in 1994 (Fig. 15a) was placed there because the shipboard assimilation of relatively coarse hydrographic data in a fine resolution model forecasted the existence of the vortex which was later confirmed by the drifter. Even though the drifters do not extensively sample the Ionian slope region, in a mesoscale range from the slope, several trajectories show that the steep topography and T/S fronts influence the surface currents, via eddies, meanders or wave packets.

Based on these drifter data, at the surface, the period of revolution for the three vortices is of the order of 8–20 d. The surface residence times in these vortices are usually longer, from 10–40 d. The surface residence time in the Strait varies with the deployment locations; the shortest is about 15–20 d, for the drifters remaining in the main AIS branch. All these values agree with our estimates of surface velocity (e.g. Figs. 4, 5 and 10a) and velocity scales (Section 4.2).

During Aug.–Sep. 96 (Fig. 15b), the AIS first bifurcates in the Strait near (36.5N, 12.5E) when it reaches the trench past Pantelleria (Fig. 2). Several drifters arrive at that location about 5 – 10 d after their deployments on Aug. 13–14 and the bifurcation agrees with the velocity vectors on

Aug. 22 (Fig. 4c). Later, the drifters (Fig. 15b) and our time-sequence (Figs. 4 and 5, Section 3) also agree on the strength and path of the AIS branches: the main branch goes around the ABV, MCC and ISV, while the other, much more weak and sluggish (higher density of squares on Fig. 15b), turns westward towards Tunisia and then meanders south–southeastward towards Libya. The agreement is detailed; for example, the northeastward topographically induced kink of two drifters when they reach the Ionian slope south of the ISV near (36N, 15.5E) and their subsequent entrainment in a southeastward branch of the AIS into the Ionian agrees with the corresponding flow field estimates (see Aug. 31–Sep. 7 on Figs. 5b–d). The eddying and wave patterns which several drifters follow above the Ionian slope (Fig. 15) occur after Sep. 18 (Fig. 10a) and beyond the forecasting experiment. Even though a synoptic comparison cannot be carried out, these patterns confirm the important mesoscale kinetic variability at the surface in the region (Sections 3.3 and 4). Similarly in 1994 (Fig. 15a), the trajectories in the ISV and MRV above the northern Ionian slope present several mesoscale oscillations in statistical accord with these of Section 4.2.

7. Summary and conclusions

The main features of dominant mesoscale variability in the Strait of Sicily during the summer of 1996 have been defined and described, and several hydrographic and dynamical properties of the flow and variabilities discussed. The features were identified based on two independent analyses carried out in real-time: a subjective evaluation and study of physical field estimates and their variations, and an objective estimation and forecast of the principal components of the variability. Each analysis combined the intensive data survey collected during the operation Rapid Response 96 with a numerical primitive equation model calibrated based on previous experiments in the region. We found interesting that the variability was well described by the eyes of both the subjective and objective beholders.

The properties of the physical fields and variability principal components were described and evaluated by comparisons with the surface nowcasts of the in situ data and satellite SST images. The dominant variations of the three-dimensional potential and kinetic energies were associated with five features: the Adventure Bank Vortex (ABV), Maltese Channel Crest (MCC), Ionian Shelfbreak Vortex (ISV), Messina Rise Vortex (MRV), and temperature and salinity fronts of the Ionian slope (ISFs) with their meanders and topographic wave patterns. All of these features and their variations have links with the meanders of the AIS as it flows through and out of the Strait, predominantly conserving potential vorticity. The characteristic scales of each state variable, and their standard deviations, were estimated for each of the five features. Trajectories of surface drifters were employed for synoptical and statistical confirmation of the estimates and results obtained. We also looked at sea surface height anomaly fields obtained by objective analysis of historical satellite data (e.g. Askari 1998; Ayoub et al., 1998; Nardelli et al., 1999): on several occurrences, there is a depression in sea surface height anomaly at the location of the cyclonic vortices we revealed (ABV, ISV and MRV). On Fig. 16a, a cartoon representing the dominant hydrographic and circulation features found is superposed on the satellite SST of Sep. 17, 1996. The remainder of this Section comprehensively overviews and discusses the: general circulation and dynamical properties; bifurcations of the AIS; roles of atmospheric and internal forcings;

(a): Surface circulation, hydrographic features and MAW paths
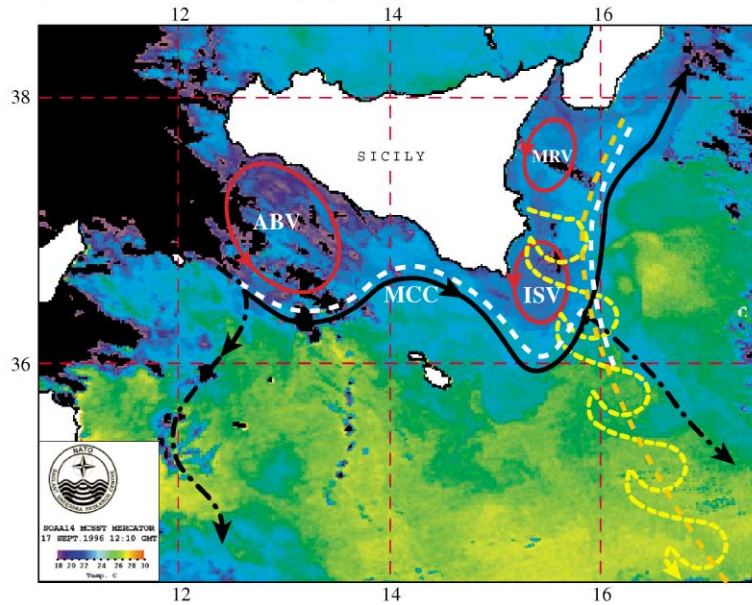
(b): IW paths
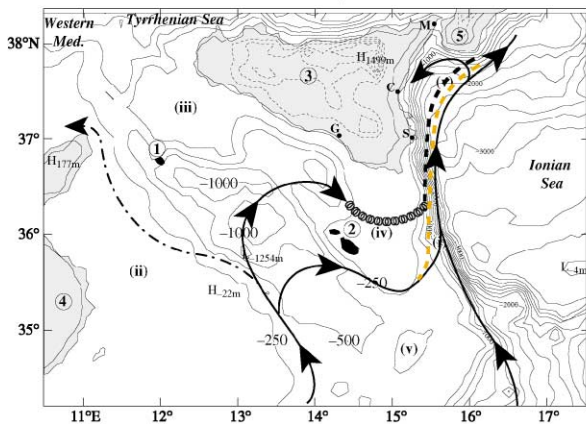
(c): LIW paths
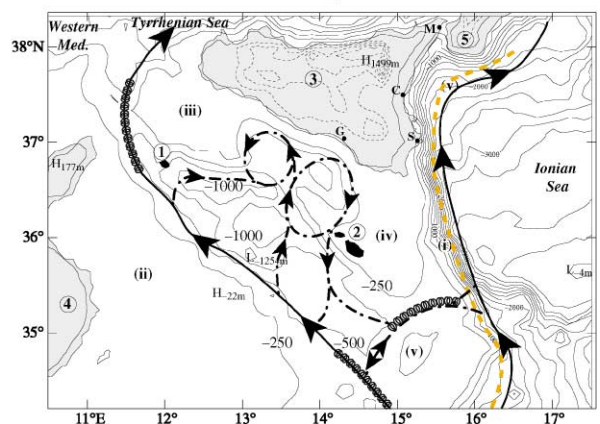
Fig. 16. Cartoons. (a) Main hydrographic and circulation features superposed on the satellite SST for Sep. 17, 1996. (b) Main IW pathways, superposed on the tography. (c) As (b), but for the LIW. On (a), the surface currents of cyclonic vortices (ABV, ISV and MRV) are schematized in red, those of the MCC and of the AIS and its branches are in black. These circulation patterns determine the main pathways of the upper-layer MAW. The sub-surface T and S fronts of the Ionian slope (ISFs) are dashed-white and dashed-orange, respectively (on b, the T front appears as dashed-black). The corresponding possible wave packets are dashed-yellow. For all Panels, dominant branches or pathways are solid lines, weaker or intermittent ones are dash-dotted. Important mixing regions are represented by corkscrews.

Even though cartoons purposely simplify reality, several properties are maintained. For example, since the S dominated Ionian slope front is tilted with depth, the largest upper-layer velocities are usually on its eastern side. The size of vortices, locations of AIS branches around Sep. 17 and dominant wavelength of possible Ionian slope wave packets are also respected (Panel a). Some properties are however not represented: e.g. compared to the MAW, the IW and LIW correspond to a broad overflow (see Figs. 12 and 13). In passing, note the agreement between the forecast for Sep. 18 (Fig. 10a) and the satellite SST.

factors controlling the ABV, MCC and ISV; interactions of the MRV and ISV; and properties of the ISFs.

General circulation. We estimated and described the predominant circulation patterns, pathways and transformations of three water masses significantly involved with the mesoscale dynamics: the upper-layer MAW and IW, and mid-depth to bottom LIW. For each of these waters, a representative σ_θ value was determined. Ranges of T, S, depth, horizontal velocity and residence times were estimated, and the spatial and some temporal variations of these ranges discussed. Several important mechanisms by which these waters transform as they circulate in the region were described. The cartoons on Fig. 16 summarize the main pathways. These of the MAW, noticeable at the surface, correspond to the main AIS and its weaker, intermittent branches (Fig. 16a). The main IW pathways (Fig. 16b) consist of a tongue in the central region of the Strait and of a meandering northward current along the Ionian slope; the overflow of IW in the western Mediterranean was found to be weak. The LIW (Fig. 16c) broadly rises above the Ionian slope. This leads to a northward boundary current along the slope which re-circulates parts of the LIW back into the Ionian Sea. The westward LIW passage is around Medina Bank, south of Malta. Once in the Strait, the westward advection continues along the Tunisian slope, with re-circulations around lenses and boundaries of local trenches. The LIW finally slides into the Tyrrenian Sea, forming an eastward boundary current.

General dynamical properties. The variations of the phase and structure of the above features were found to be somewhat larger and faster than previous estimates in the region based on data local in space or time (Section 1.1). For example, at the surface, they involved shifts of about 20–100 km, usually occurring within 2–4 d. The mesoscale standard deviation of the vertically averaged transport through the Strait was estimated in the ± 0.1–0.2 Sv range; that of the transport along the Ionian slope was about ± 1 Sv.

   Most hydrographic anomalies have a large subsurface signature near the main thermocline and halocline surfaces. For the features directly linked to the upper-layer MAW, i.e. the ABV, MCC, ISV and MRV, important changes can also be identified from the surface T. This surface identification is more challenging for the ISFs since their meanders and wave patterns mainly correspond to subsurface hydrographic variations. Most velocity anomalies are important in the surface layers since field variations are close to thermal-wind balance and velocities are usually small at depth. For the features in the Strait, the main variability is baroclinic, but near the Ionian slope, both barotropic and baroclinic processes can be important. Overall, it was found that topographic effects and internal dynamics are as important as upwellings in the control of the surface-intensified features.

AIS and its bifurcations. Based on the estimated fields and independent surface drifter data, the bifurcations of the AIS were found related to steep topographic features and to density gradients overlaying these features (Fig. 16a). Once in the Strait, the first bifurcation occurs when the stream reaches the trench past Pantelleria near (36.5N, 12.5E). Subsequently, the main AIS veers to the north–northeast, meandering around the ABV, MCC and ISV, while the weaker and more sluggish southern branch meanders along the Tunisian shelf. This first bifurcation and the opposite subsurface tongue of core IW (Figs. 12 and 16b) explain the warmer and saltier waters

observed in the central part of the Strait, southwest of Malta. The second bifurcation of the main AIS occurs above the Ionian slope near (36.2N, 16E). The main AIS branch continues to the north, along the Ionian slope, bordering the MRV and Calabria. The weaker southern branch is variable in strength and direction: initially during Aug. 22–28, it flowed eastward into the Ionian Sea (e.g. Fig. 1), but starting around Sep. 7, it flowed to the southeast along the Ionian slope (e.g. Fig. 16).

Atmospheric and internal forcings. Two similar wind events of adequate direction and sufficient strength and duration (e.g. storms with 3 d of westerly wind stress around 1 dyn/cm^2, Section 3.3) were observed to establish similar circulation and buoyancy variations that could persist for several days. Strong enough synoptic atmospheric forcing can thus control the regional variability. After weaker or more variable atmospheric conditions, even though ocean snapshots were shown to usually differ, they were sometimes found similar. Internal dynamical events can thus also control the regional variability, confirming suggestions of Manzella et al. (1990). For example, the frequent lack of upwelling at the Gulf of Gela (Piccioni et al., 1988) was found here to be due to the MCC.

ABV, MCC and ISV. The field and variability estimates suggested that the factors favoring permanent ABV, MCC and ISV during the summer period were: (1) topography, i.e. the squeezing and stretching of the AIS over the Adventure Bank and Maltese plateau; (2) atmospheric forcing (summer winds predominantly westerly when significant), i.e. the coastal upwelling and associated buoyancy currents funneling the AIS offshore; and (3) inertia, i.e. the potential and kinetic energies stored in the isopycnal domes of the ABV and ISV once they are formed. Overall, the meanders of the main AIS are also maintained by these three factors.

MRV and ISV. Our estimates showed that for periods of a few days to a week, the MRV, and in a lesser extent, the ISV, could become weak, suggesting intermittency. For the MRV, considering the above controlling factors, on its offshore side, one reason for intermittency is the lack of strong topographic veering effects that the ABV and ISV have (see Fig. 2). The coastal side of the MRV may also be unsettled by advection of relatively heavy IW (Fig. 16b) or by meandering southward shelf currents (Böhm et al., 1987) whose origins have been suggested to be tidal-mixing near the sill of the Strait of Messina (Lavenia and Pisani, 1974; Alpers and Salusti, 1983). The MRV can finally lack the necessary strong wind inputs: for the present period, it seemed to require winds of sufficiently strong northerly component to establish, by downwelling, a coherent stream on its coastal side (e.g. Section 3). After a wind event, inertia can maintain this coherence, for some time.

For the ISV, in addition to the less favorable coastal geometry than the ABV (Fig. 2), its weaker periods or oscillations are likely related to internal dynamics at the Ionian slope and to atmospheric responses on the eastern coast of Sicily. In fact, for periods lasting a few days or more, the variations of the MRV and ISV were observed to be in phase. Internally, the variability principal components suggested that an interactive behavior is favored by wave packets and meanders of the ISFs. Externally, on two occurrences, wind events of strong enough northerly component were observed to amplify the coastal sides of the ISV and MRV simultaneously

(Section 3). In general, depending on the dominant phase and scales of the wave packets and frontal meanders, and on the wind direction, the ISV and MRV can either be mutually strengthened or weakened.

ISFs. During Aug.–Sep. 1996, mesoscale processes near the Ionian slope were estimated to account for about 50% of the normalized physical variability occurring in our domain (Fig. 2). Guided by the corresponding variability principal components and standard deviations, two along-slope fronts were revealed: one T dominated, one S dominated. These T and S slope fronts were found to prevail at different locations and depths (Fig. 16, Sections 4.2 and 5), in relation to the (i) upper-layer advection of MAW by the main AIS north of about 36N, and (ii), mid-depth rising of the LIW above the Ionian shelfbreak south of about 37N. As drawn on Fig. 16, the upper-layer T front is mainly to the north of 36N, but the mid-depth S front, being maintained to the north by inertia of the slope current, runs along the whole slope (at a given depth, along the portion of the slope intersecting that depth). Previously, only the upper layers of the region where these fronts overlap had been studied at the mesoscale (e.g. Briscoe et al., 1974). The two fronts lead to a vertically averaged anticyclonic circulation along the slope (in our domain, up to Calabria), with a northward barotropic transport at about 3.5 Sv. The northward circulation agrees with previous Ionian data (Nittis et al., 1993; Malanotte-Rizzoli et al., 1999), excepted that here, a bifurcation of the AIS is estimated to occur directly over the slope, near (36.2N, 16E).

Using the estimated fields, their tendencies, and the principal components of the normalized variability, several properties of the mesoscale dynamics along the slope were obtained. The main horizontal space-scales are near 25 km (wavelength near 150 km), the main time-scales range from the inertial period to several days (real ocean wave packets and meanders interact on multiple scales surrounding these values). The largest T and S anomalies are in the thermocline of the MAW and upper halocline of the LIW, respectively. The largest velocity anomalies are close to thermal-wind balance and dominate in the surface layers; the standard deviations in the northward $\Delta\psi$ are near ± 1 Sv. For further characterization, additional theoretical, observational and numerical simulation studies are necessary. In particular, to reduce uncertainty (Lermusiaux, 1999b), it should be useful to measure total velocity and temperature (salinity) along the temperature (salinity) dominated front (Fig. 16).

Acknowledgements

References

Alpers, W., Salusti, E., 1983. Scylla and Charybdis observed from space. Journal of Geophysical Research 88 (C3), 1800–1808.

Angeluci, M.G., Pinardi, N., 1997. Analysis of 1987–94 ECMWF meteorological fields in the Mediterranean region, Part II: surface fields. IMGA Report 3/1997.

Artale, V., Provenzale, A., Santoleri, R., 1989. Analysis of internal temperature oscillations of tidal period on the Sicilian continental shelf. Continental Shelf Research 9 (10), 867–888.

Artegiani, A., Bregant, D., Paschini, E., Pinardi, N., Raicich, F., Russo, A., 1997. The Adriatic Sea general circulation. Part I: Air-sea interactions and water mass structure. Journal of Physical Oceanography 27, 1492–1514.

Askari, F., 1998. Remote sensing of topographically-induced upwelling in the southern coastal region of Sicily. Saclantcen Report: SR-282, Saclantcen, La Spezia, Italy, pp. 1–24.

Astraldi, M., Balopoulos, S., Candela, J., Font, J., Gacic, M., Gasparini, G.P., Manca, B., Theocharis, A., Tintoré, J., 1999. The role of straits and channels in understanding the characteristics of Mediterranean circulation. Progress in Oceanography 44 (1–3), 65–108.

Ayoub, N., Le Traon, P.-Y., De Mey, P., 1998. A description of the Mediterranean surface variable circulation from combined ERS-1 and TOPEX/POSEIDON altimetric data. In Special Issue: Mediterranean eddy resolving modeling and Interdisciplinary studies (MERMAIDS). Journal of Marine Systems 18 (1–3), 3–40.

Böhm, E., Magazzu, G., Wald, L., Zoccolotti, M.-L., 1987. Coastal currents on the Sicilian shelf south of Messina. Oceanologica Acta 10 (2), 137–142.

Borzelli, G., Ligi, R., 1999a. Empirical orthogonal function analysis of SST image series: a physical interpretation. Journal of Atmospheric and Oceanic Technology 16, 682–690.

Borzelli, G., Ligi, R., 1999b. Autocorrelation scales of the SST distribution and water masses stratification in the Channel of Sicily. Journal of Atmospheric and Oceanic Technology 16, 776–781.

Brankart, J.M., Brasseur, P., 1996. Optimal analysis of in situ data in the Western Mediterranean using statistics and cross-validation. Journal of Atmospheric and Oceanic Technology 16 (2), 477–491.

Briscoe, M.G., Johannessen, O.M., Vincenzi, S., 1974. The Maltese oceanic front: a surface description by ship and aircraft. Deep-Sea Research 21, 247–262.

Candela, J., Mazzola, S., Sammari, C., Limeburner, R., Lozano, C.J., Patti, B., Bonnano, A., 1999. The "Mad Sea" phenomenon in the Strait of Sicily. Journal of Physical Oceanography 29, 2210–2231.

Cane, M.A., Kamenkovich, V.M., Krupitsky, A., 1998. On the utility and disutility of JEBAR. Journal of Physical Oceanography 28 (3), 519–526.

Curchister, E.N., Haidevogel, D.B., Iskandarani, M., 1999. On the transient adjustment of a mid-latitude abyssal ocean basin with realistic geometry: the constant depth limit. Dynamics of Atmospheres and Oceans (Special issue in honor of Professor A.R. Robinson) 29, 147–188.

Cushman-Roisin, B., 1994. Introduction to Physical Oceanography. Prentice-Hall, Inc., Englewood Cliffs, NJ.

Daley, R., 1992. Estimating model-error covariances for application to atmospheric data assimilation. Monthly Weather Review 120, 1735–1746.

De Agostini Institute, 1998. Atlante geografico metodico De Agostini. Officine Grafiche De Agostini, Novana, 272pp.

Gacic, M., Astraldi, M., La Violette, P.E., 1999. The Mediterranean Sea — Circulation, strait exchange and dense water formation processes — Preface. Journal of Marine Systems 20 (1–4), VII–IX.

Gill, A.E., 1982. Atmosphere-Ocean Dynamics. International Geophysics Series, Vol. 30, Academic Press, New York.

Graham, A., 1981. Kronecker Products and Matrix Calculus: with Applications. Ellis Horwood, Limited, Chichester Halsted Press, New York, (a division of Wiley, New York).

Grancini, G.F., Michelato, A., 1987. Current structure and variability in the Strait of Sicily and adjacent area. Annales Geophysicae, Series B (Terrestrial and Planetary Physics) 5 (1), 75–88.

Herbaut, C., Codron, F., Crepon, M., 1998. Separation of a coastal current at a strait level: case of the Strait of Sicily. Journal of Physical Oceanography 28 (7), 1346–1362.

Hua, B.L., McWilliams, J.C., Owens, W.B., 1986. An objective analysis of the POLYMODE local dynamics experiment. Part II: Streamfunction and potential vorticity fields during the intensive period. Journal of Physical Oceanography 16, 506–522.

Janowitz, G.S., Pietrafesa, L.J., 1982. The effects of alongshore variations in bottom topography on a boundary current, or, topographically induced upwelling. Continental Shelf Research 1, 123–141.

Killworth, P.D., 1983. On the motion of isolated lenses on a beta-plane. Journal of Physical Oceanography 13, 368–376.

Killworth, P.D., Blundell, J.R., Dewar, W.K., 1997. Primitive equation instability of wide oceanic rings. I. Linear theory. Journal of Physical Oceanography 27 (6), 941–962.

Kundu, P.K., 1990. Fluid Mechanics. Academic Press, Inc., New York, 638pp.

Lavenia, A., Pisani, M., 1974. Observation of surface temperature in some areas of the Mediterranean in the summer and autumn of 1968. Bollettino di Geofisica Teorica ed Applicada 16 (61), 39–50.

La Violette, P.E. (Ed.), 1994a. Coastal and Estuarine Studies 46: Seasonal and Interannual Variability of the Western Mediterranean Sea. AGU, Washington, DC.

La Violette, P.E., 1994b. Overview of the major forcings and water masses of the Western Mediterranean Sea. In: La Violette, P.E., (Ed.), Coastal and Estuarine Studies 46: Seasonal and Interannual Variability of the Western Mediterranean Sea. AGU, Washington DC, pp. 1–11.

Lermusiaux, P.F.J., 1997. Error subspace data assimilation methods for ocean field estimation: theory, validation and applications. Ph.D. Thesis, May, Harvard Univ., Cambridge, MA.

Lermusiaux, P.F.J., 1999a. Data assimilation via error subspace statistical estimation, Part II: Middle Atlantic Bight shelfbreak front simulations and ESSE validation. Monthly Weather Review 127 (7), 1408–1432.

Lermusiaux, P.F.J., 1999b. Estimation and study of mesoscale variability in the Strait of Sicily. Dynamics of Atmospheric Oceans (Special issue in honor of Professor A.R. Robinson) 29, 255–303.

Lermusiaux, P.F.J., Anderson, D.G., Lozano, C.J., 2000. On the mapping of multivariate geophysical fields: error and variability subspace estimates. Quarterly Journal of the Royal Meteorological Society B 1387–1430.

Lermusiaux, P.F.J., Robinson, A.R., 1999. Data assimilation via error subspace statistical estimation, Part I: theory and schemes. Monthly Weather Review 127 (7), 1385–1407.

Lipiatou, E., Heussner, S., Mosetti, R., Tintore, J., Tselepides, A. (Eds.), 1999. Progress in oceanography of the Mediterranean Sea. (Special issue). Progress in Oceanography 44 (1–3), 1–468.

Louis, A.K., Maass, P., Rieder, A., 1997. Wavelets Theory and Applications. Pure and Applied mathematics, A Wiley-Interscience Series of Texts, Monographs and Tracts. Wiley, New York.

Lozano, C.J., Robinson, A.R., Arango, H.G., Gangopadhyay, A., Sloan, N.Q., Haley, P.J., Leslie, W.G., 1996. An interdisciplinary ocean prediction system: assimilation strategies and structured data models. In: Malanotte-Rizzoli, P., (Ed.), Modern Approaches to Data Assimilation in Oceano Modelling, Elsevier Oceanography Series, Elsevier Science, The Netherlands.

Lynch, D.R., Davies, A.M., Gerritsen, H., Mooers, C.N.K., 1995. Closure: quantitative skill assessment for coastal ocean models. In: Coastal and Estuarine Studies. D.R. Lynch and A.M. Davies (Eds.) Am. Geophys. Union, Washington DC, pp. 501–506.

Malanotte-Rizzoli, P., Manca, B.B., d'Alcala, M.R., Theocharis, A., Bergamasco, A., Bregant, D., Budillon, G., Civitarese, G., Georgopoulos, D., Michelato, A., Samsone, E., Scarazzato, P., Souvermezoglou, E., 1997. A synthesis of the Ionian Sea hydrography, circulation and water mass pathways during POEM-Phase I. Progress in Oceanography 39, 153–204.

Malanotte-Rizzoli, P., Manca, B.B., d'Alcala, M.R., Theocharis, A., Brenner, S., Budillon, G., Ozsoy, E., 1999. The Eastern Mediterranean in the 80s and in the 90s: the big transition in the intermediate and deep circulations. Dynamics of Atmospherics and Oceans (Special issue in honor of Prof. A.R. Robinson) 29, 365–395.

Malanotte-Rizzoli, P., Robinson, A.R. (Eds.), 1994. Ocean Processes in Climate Dynamics: Global and Mediterranean Examples. NATO-ASI Series C: Mathematical and Physical Sciences, Vol. 419. Kluwer Academic Publishers, Dordrecht.

Manzella, G.M.R., 1994. The seasonal variability of the water masses and transport through the Strait of Sicily. In: La Violette, P.E., (Ed.), Coastal and estuarine studies 46: Seasonal and Interannual Variability of the Western Mediterranean Sea, AGU. Washington DC, pp. 33–45.

Manzella, G.M.R., Gasparini, G.P., Astraldi, M., 1988. Water exchange between the eastern and western Mediterranean through the Strait of Sicily. Deep-Sea Research 35, 1035–1121.

Manzella, G.M.R., Hopkins, T.S., Minnett, P.J., Nacini, E., 1990. Atlantic Water in the Strait of Sicily. Journal of Geophysical Research 95 (C2), 1569–1575.

Manzella, G.M.R., La Violette, P.E., 1990. The seasonal variation of water mass content in the Western Mediterranean and its relationship with the inflows through the straits of Gibraltar and Sicily. Journal of Geophysical Research 95 (C2), 1623–1626.

Marani, M., Argnani, A., Roveri, M., Trincardi, F., 1993. Sediment drifts and erosional surfaces in the central Mediterranean: seismic evidence of bottom-current activity. Sedimentary Geology 82, 207–220.

Miller, A.J., Lermusiaux, P.F.J., Poulain, P.M., 1996. A Topographic-Rossby Mode Resonance over the Iceland-Faeroe Ridge. Journal of Physical Oceanography 26 (12), 2735–2747.

Milliff, R.F., Robinson, A.R., 1992. Structure and dynamics of the Rhodes Gyre System and dynamical interpolation for estimates of the mesoscale variability. Journal of Physical Oceanography 22 (4), 317–337.

Molines, J.-M., 1991. Modelling the barotropic tides in the Strait of Sicily and Tunisian shelf. Oceanologica Acta 14 (3), 241–252.

Monin, A.S., 1990. Theoretical Geophysical Fluid Dynamics. Kluwer Academic Publishers, Dordrecht.

Mosetti, F., Purga, N., 1989. The semi-diurnal tides in the Sicily Strait. Nuovo Cimento C Series 1 12C (3), 349–356.

Moretti, M., Sansone, E., Spezie, G., De Maio, A., 1993. Results of investigations in the Sicily Channel (1986–1990). Deep-Sea Research II 40 (6), 1181–1192.

Nardelli, B.B., Santoleri, R., Iudicome, D., Zoffoli, S., Marullo, S., 1999. Altimetric signal and three-dimensional structure of the sea in the Channel of Sicily. Journal of Geophysical Research 104 (C9), 20,585–20,603.

Nihoul, J.C.J., Djenidi, S., 1998. Coupled physical, chemical and biological models. In: Brink, K.H., Robinson, A.R., (Eds.), The Sea: The Global Coastal Ocean I, Processes and Methods, Vol. 10. Wiley, New York, NY.

Nittis, K., Pinardi, N., Lascaratos, A., 1993. Characteristics of the summer 1987 flow field in the Ionian Sea. Journal of Geophysical Research 98, 10,171–10,184.

Onken, R., Sellschopp, J., 1998. Seasonal variability of flow instabilities in the Strait of Sicily. Journal of Geophysical Research 103 (C11), 24,799–24,820.

Orlanski, I., 1976. A simple boundary condition for unbounded hyperbolic flows. Journal of Computational Physics 41, 251–269.

Ozturgut, E., 1975. Temporal and spatial variability of water masses: the Strait of Sicily (MEDMILOC 72). Saclantcen Memo: SM-65, Saclantcen, La Spezia, Italy, pp. 1–26.

Pedlosky, J., 1987. Geophysical Fluid Dynamics, 2nd Edition. Springer, Berlin.

Philippe, M., Harang, L., 1982. Surface temperature fronts in the Mediterranean Sea from infrared satellite imagery. In: Nihoul, J.C.J. (Ed.), Hydrodynamics of Semi-Enclosed Seas, Elsevier, New York, pp. 91–128.

Piccioni, A., Gabriele, M., Salusti, E., Zambianchi, E., 1988. Wind-induced upwellings off the southern coast of Sicily. Oceanologica Acta 11 (4), 309–314.

Pierini, S., 1996. Topographic Rossby modes in the Strait of Sicily. Journal of Geophysical Research 101 (C3), 6429–6440.

Pinardi, N., Korres, G., Lascaratos, A., Roussenov, V., Stanev, E., 1997. Numerical simulation of the interannual variability of the Mediterranean Sea upper ocean circulation. Geophysical Research Letters 24 (4), 425–428.

Pinardi, N., Roether, W. (Eds.), 1998. Mediterranean eddy resolving modelling and interdisciplinary studies (MER-MAIDS) (Special issue). Journal of Marine Systems 18 (1–3), 1–312.

Poulain, P.-M., 1999. Drifter observations of surface circulation in the Adriatic Sea between December 1994 and March 1996. Journal of Marine Systems 20, 231–253.

Poulain, P.-M., 2001. Adriatic Sea surface circulation as derived from drifter data between 1990 and 1999. Journal of Marine Systems, in press.

Pouliquen, E., Kirwan, A.D., Pearson, R.T. (Eds.), 1997. Rapid Environmental Assessment, Saclantcen conference proceedings series CP-44, Saclantcen, La Spezia, Italy, 290pp.

Preisendorfer, R.W., 1988. Principal Component Analysis in Meteorology and Oceanography. Elsevier, Amsterdam.

Robinson, A.R., 1996. Physical processes, field estimation and an approach to interdisciplinary ocean modeling. Earth-Science Reviews 40, 3–54.

Robinson, A.R., 1997. Forecasting and simulating coastal ocean processes and variabilities with the Harvard Ocean Prediction System. In: Pouliquen, E. (Ed.), Rapid Environmental Assessment, Saclantcen Conference Proceedings Series CP-44, Saclantcen, La Spezia, Italy, 290pp.

Robinson, A.R., 1999. Forecasting and simulating coastal ocean processes and variabilities with the Harvard Ocean Prediction System. In: Mooers, C.N.K. (Ed.), Coastal Ocean Prediction, AGU Coastal and Estuarine Studies Series. AGU, Washington, DC, pp. 77–100.

Robinson, A.R., Arango, H.G., Warn-Varnas, A., Leslie, W.G., Miller, A.J., Haley, P.J., Lozano, C.J., 1996. Real-time regional forecasting. In: Malanotte-Rizzoli, P. (Ed.), Modern Approaches to Data Assimilation in Ocean Modeling, Elsevier Science, B.V, Amsterdam.

Robinson, A.R., Glenn, S.M., 1999. Adaptive sampling for ocean forecasting. Naval Research Reviews 51 (2), 28–38.

Robinson, A.R., Golnaraghi, M., 1994. The physical and dynamical oceanography of the Mediterranean Sea. In: Ocean Processes in Climate Dynamics: Global and Mediterranean Examples, NATO-ASI Series C: Mathematical and Physical Sciences Vol. 419. Kluwer Academic Publishers, Dordrecht, pp. 255–306.

Robinson, A.R., Golnaraghi, M., Leslie, W.G., Artegiani, A., Hecht, A., Lazzoni, E., Michelato, A., Sansone, E., Theocharis, A., Ünlüata, Ü., 1991. The eastern Mediterranean general circulation: Features, structure and variability. Dynamics of Atmospheres and Oceans 15 (3–5), 215–240.

Robinson, A.R., Lermusiaux, P.F.J., Sloan III, N.Q., 1998a. Data assimilation. In: Brink, K.H., Robinson, A.R. (Eds.), The Sea: The Global Coastal Ocean I, Processes and Methods, Vol. 10. Wiley, New York, NY.

Robinson, A.R., Leslie, W.G., 1985. Estimation and Prediction of Oceanic Fields. Progress in Oceanography 14, 485–510.

Robinson, A.R., Malanotte-Rizzoli, P. (Guest Eds.), 1993. Topical studies in oceanography: physical oceanography of the eastern Mediterranean Sea. Deep-Sea Research II 40 (6), 1073–1329.

Robinson, A.R., Sellschopp, J., Warn-Varnas, A., Leslie, W.G., Lozano, C.J., Haley Jr., P.J., Anderson, L.A., Lermusiaux, P.F.J., 1999. The Atlantic Ionian Stream. Journal of Marine Systems 20, 129–156.

Robinson, A.R., Walstad, L.J., 1987. The Harvard Open Ocean Model: calibration and application to dynamical process, forecasting, and data assimilation Studies. Journal of Applied Numerical Mathematics 3 (1–2), 89–131.

Robinson, A.R., Haley Jr, P.J., Lermusiaux, P.F.J., Leslie, W.G., Lozano, C.J., Anderson, L.A. and Dusenberry, J.A., 1998b. The Rapid Response 96, 97 and 98 exercises: the Strait of Sicily, Ionian Sea and Gulf of Cadiz. Harvard open ocean model reports, Reports in Meteorology and Oceanography, N. 57.

Sasaki, Y., 1970. Some basic formalism in numerical variational analysis. Monthly Weather Review 98, 875–883.

Sellschopp, J., Robinson, A.R., 1997. Describing and forecasting ocean conditions during operation rapid response. In: Pouliquen, E., (Ed.), Rapid Environmental Assessment, Saclantcen Conference Proceedings Series CP-44, Saclantcen, La Spezia, Italy, 290pp.

Simpson, J.H., 1998. Tidal processes in shelf seas. In: Brink, K.H., Robinson, A.R. (Eds.), The Sea: The Global Coastal Ocean I, Processes and Methods, Vol. 10. Wiley, New York, NY.

Spall, M.A., Robinson, R.A., 1989. A new open ocean, hybrid coordinate primitive equation model. Mathematics and Computers in Simulation 31, 241–269.

Sparnocchia, S., Gasparini, G.P., Astraldi M., Borghini, M., Pistek, P., 1999. Dynamics and mixing of the Eastern Mediterranean outflow in the Tyrrhenian basin. Journal of Marine Systems, (1–4), 301–317.

Tarantola, A., 1987. Inverse Problem Theory. Methods for Data Fitting and Model Parameter Estimation. Elsevier Science Publishers, Amsterdam, The Netherlands.

von Storch, Frankignoul, H.C., 1998. Empirical modal decomposition in coastal oceanography. In: Brink, K.H., Robinson, A.R. (Eds.), The Sea: The Global Coastal Ocean I, Processes and Methods, Vol. 10. Wiley, New York, NY.

Warn-Varnas, A., Sellschopp, J., Haley Jr., P.J., Leslie, W.G., Lozano, C.J., 1999. Strait of Sicily Water Masses. Dynamics of Atmospheres and Oceans (Special issue in honor of Professor A.R. Robinson) 29, 437–469.

Zavatarelli, M., Mellor, G.L., 1995. A numerical study of the Mediterranean Sea circulation. Journal of Physical Oceanography 25 (6), 1384–1414.